

# Wide-field optical eye models for emmetropic and myopic eyes

**Gareth D. Hastings**

Herbert Wertheim School of Optometry and Vision Science, University of California Berkeley, Berkeley, CA, USA



**Pavan Tiruveedhula**

Herbert Wertheim School of Optometry and Vision Science, University of California Berkeley, Berkeley, CA, USA



**Austin Roorda**

Herbert Wertheim School of Optometry and Vision Science, University of California Berkeley, Berkeley, CA, USA



Ocular wavefront aberrations are used to describe retinal image formation in the study and modeling of foveal and peripheral visual functions and visual development. However, classical eye models generate aberration structures that generally do not resemble those of actual eyes, and simplifications such as rotationally symmetric and coaxial surfaces limit the usefulness of many modern eye models. Drawing on wide-field ocular wavefront aberrations measured previously by five laboratories, 28 emmetropic (−0.50 to +0.50 D) and 20 myopic (−1.50 to −4.50 D) individual optical eye models were reverse-engineered by optical design ray-tracing software. This involved an error function that manipulated 27 anatomical parameters, such as curvatures, asphericities, thicknesses, tilts, and translations—constrained within anatomical limits—to drive the output aberrations of each model to agree with the input (measured) aberrations. From those resultant anatomical parameters, three representative eye models were also defined: an *ideal emmetropic eye* with minimal aberrations (0.00 D), as well as a *typical emmetropic eye* (−0.02 D) and *myopic eye* (−2.75 D). The cohorts and individual models are presented and evaluated in terms of output aberrations and established population expectations, such as Seidel aberration theory and ocular chromatic aberrations. Presented applications of the models include the effect of dual focus contact lenses on peripheral optical quality, the comparison of ophthalmic correction modalities, and the projection of object space across the retina during accommodation.

## Introduction

Visual perception and ocular development are considerably dependent on the quality of the retinal image, which, in the absence of pathology, is primarily determined by ocular optics and retinal shape. Foveal optics are classically relevant to fixated vision, whereas peripheral optics (across the retina; beyond the fovea) are of burgeoning interest given their importance in accommodation (Labhishetty, Cholewiak, & Banks, 2019), mobility (Patino et al., 2010), driving (Wood & Troutbeck, 1992), and associations with the onset and progression of myopia (Smith, Hung, & Huang, 2009). Hence, peripheral image quality is increasingly being evaluated in the design of spectacle lenses (Bowrey et al., 2017; Sankaridurg et al., 2010), contact lenses (Kang, Gifford, & Swarbrick, 2013), intraocular lenses (Villegas et al., 2022), and near-eye displays (Yang et al., 2013). The most comprehensive descriptor of ocular optics is wavefront sensing, which captures the combined interactions of all the ocular refracting surfaces and media with the effect of retinal shape. The present work sought to develop optical eye models that plausibly resembled ocular anatomy and reproduce measured ocular wavefront aberrations both at the fovea and across a wide-field extent of the visual field.

Dozens of eye models have been proposed over hundreds of years—see Atchison and Thibos (2016) for a historical review. The predominant approach has been to define ocular refracting surfaces and media based on measured or modeled anatomical biometry and to update preceding models whenever a particular ocular structure or refractive index could be better

Citation: Hastings, G. D., Tiruveedhula, P., & Roorda, A. (2024). Wide-field optical eye models for emmetropic and myopic eyes. *Journal of Vision*, 24(7):9, 1–26, <https://doi.org/10.1167/jov.24.7.9>.



characterized by advancing imaging technology or by more sophisticated modeling. Although biometry approaches continue to improve (Marcos et al., 2021), potential drawbacks include that deeper ocular structures are imaged through more anterior structures, different anatomical structures are measured with reference to different ocular axes, and biometers are potentially confounded by the need to agree with de facto standards of regulatory boards and frequently incorporate fiducial offsets. Consequently, it has long been shown that ray tracing through classical eye models results in aberrations that do not correspond to those of actual eyes (Akram, Baraas, & Baskaran, 2018; Polans, Jaeken, McNabb, Artal, & Izatt, 2015; Pomerantzeff, Fish, Govignon, & Schepens, 1971). Indeed, the present work confirms that many anatomical and biometric parameters, such as tilts and decentrations, average to zero and result in eye models of optical quality well above the level of typical individual eyes.

With the aid of modern computing and wavefront sensing, an alternative approach is to measure ocular aberrations across the visual field and then to optimize the anatomical structures of an eye model in software, such that the measured aberrations are closely replicated when rays are traced through the model at the same field angles. In the past, this reverse-engineering approach has been used with various degrees of data pooling and anatomical simplifications, such as rotational symmetry and coaxial alignment of surfaces. The present work combines the backward design aberration technique with rotationally asymmetric, aspheric, tilted, and decentered ocular refracting and retinal surfaces to define cohorts of individual emmetropic and myopic eye models, as well as ideal and realistic average eye models.

This article first describes the input wavefront error data and the constraints and optimization of the modeling process. The resultant eye models are then presented and evaluated in terms of their output aberrations and their agreement with established population expectations such as Seidel aberration theory and ocular chromatic aberrations. Finally, some applications of the models are illustrated, including the comparison of ophthalmic correction modalities and the projection of object space across the retina during accommodation.

## Methods

### Subjects and input wavefront error datasets

Wavefront error data for 72 subjects, described using Zernike aberration coefficients, were shared by five laboratories (Liu, Sreenivasan, & Thibos, 2016; Lundström, Mira-Agudelo, & Artal, 2009; Mathur,

Atchison, & Charman, 2009; Polans et al., 2015; Pusti et al., 2023). Details of the instrument systems and measurement protocols from those original studies are summarized in Appendix A. Foveal refractive error was used to sort eyes into emmetropic and myopic groups and was calculated using second- through sixth-order radially symmetric Zernike terms (Thibos, Hong, Bradley, & Applegate, 2004) after adjusting the defocus coefficient from the measured wavelength, which ranged from 555 to 850 nm (Appendix A) to 555 nm using a model of human ocular chromatic aberration (Thibos, Ye, Zhang, & Bradley, 1992). Changes in higher-order aberrations with wavelength are not uniform (Nam, Rubinstein, & Thibos, 2010) and are, for the most part, negligible (Fernández & Artal, 2008; Llorente, Diaz-Santana, Lara-Saucedo, & Marcos, 2003; Mozaffari, LaRocca, Jaedicke, Tiruveedhula, & Roorda, 2020); therefore, no other terms were adjusted. This adjustment for chromatic aberration was used only to parse the eyes into the refractive groups; the individual eye models were optimized and evaluated (as described in the Individual eye models: Optimization) at their measured wavelengths.

At 555 nm, emmetropia was defined as a spherical refractive error between  $-0.50$  and  $+0.50$  D and myopic eyes between  $-1.5$  D and  $-4.5$  D were considered. Some eyes were excluded for being outside these refractive error ranges, as well as for their wavefront errors being measured through spectacle corrections, or for their refit circular pupil diameter being less than 4 mm at any field location.

### Field sign convention, right and left eyes, and measurements at the optic nerve head

Wavefront errors that were measured at discrete increments of visual angle over the visual field by different laboratories were mapped onto the following coordinate system for consistency: Horizontal and vertical directions are defined as  $x$  and  $y$  axes, respectively, in a plane parallel with the coronal plane. Perpendicular to that plane (essentially parallel to the optical axis of the eye) is the  $z$  axis (Figure 1). Because wavefront errors were measured at field locations defined relative to fixation, the origin (0,0) in the  $xy$  plane is the fovea or the preferred retinal locus for fixation.

Object-space field angles are defined in degrees and the sign convention is defined by the slope of a ray when it intersects with the object-space  $z$  axis at the entrance pupil. That is, rays from the inferior and left visual fields (from the perspective of an eye) have a positive slope with respect to the  $z$  axis and thus have positive field coordinates. In summary, positive field coordinates refer to the inferior visual field in both eyes,

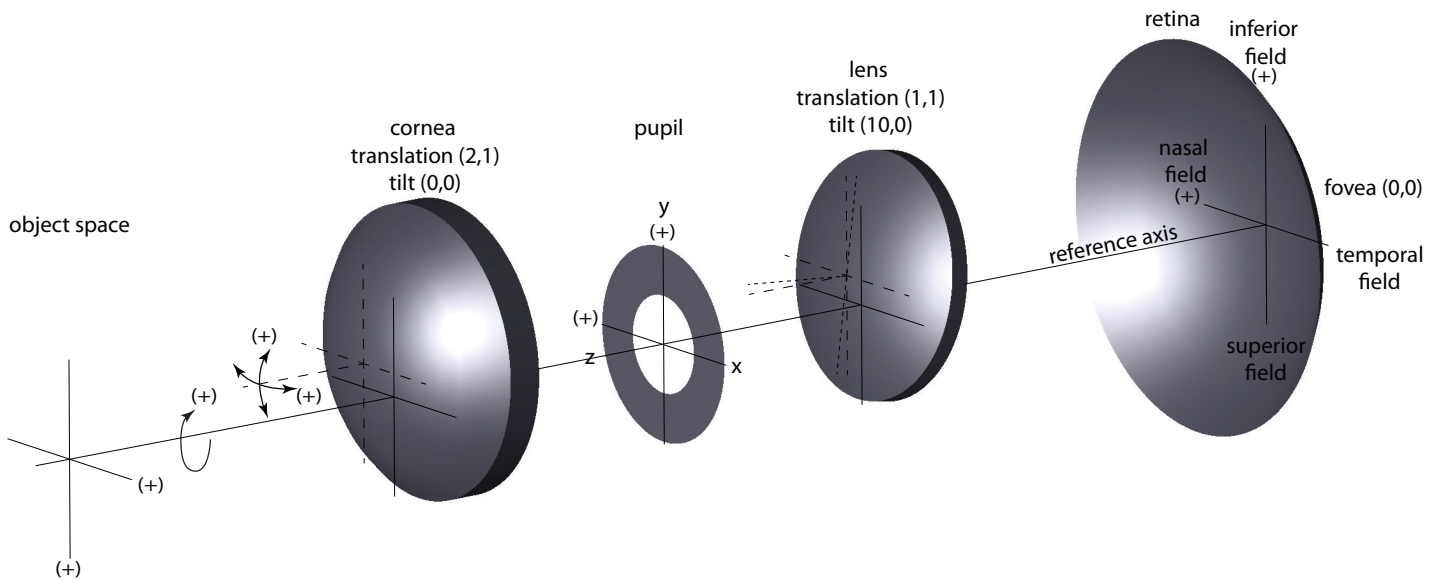


Figure 1. Coordinate system of a right eye used in the models. The anatomical elements of the model eye are separated axially for illustration purposes. The global  $x$  and  $y$  axes are drawn at each surface with solid lines. The line joining the center of the pupil to the center of the retina defines a reference axis (equivalent to the optical axis in a coaxial system). Translations, tilts, and rotations of the cornea and lens are made relative to this reference axis. The local  $x$  and  $y$  axes relative to the corneal center and the lens center are drawn with dashed lines. The illustrated lens has a second set of axes with shorter dashes to indicate an arbitrary upward pitch of  $+10^\circ$ .

the nasal field of right eyes, and the temporal field of left eyes, whereas negative field coordinates refer to the superior visual field in both eyes, the temporal field of right eyes, and the nasal field of left eyes.

No adjustment was made during optimization for data from right or left eyes; only when the output results of the models are presented are right and left eyes are pooled. Then, left eyes were adjusted in three possible ways, depending on the output being reported: signs of horizontal field coordinates were flipped to align with those of right eyes; signs of Zernike coefficients with positive odd and negative even meridional frequencies were reversed as recommended (American National Standards Institute, 2004); and optical surfaces representing rotationally asymmetric anatomical structures were mirrored about the vertical axis.

Some wavefront error data were collected using sweeping and/or automated techniques that recorded measurements over the optic nerve head (physiological blind spot); these data are not meaningful and were omitted from the data that drove the optimizations. These were any measurements falling within a  $6^\circ \times 8^\circ$  area centered at  $15^\circ$  in the temporal field and  $2^\circ$  in the inferior field (Armaly, 1969; Safran,

Mermillod, Mermoud, de Weisse, & Desangles, 1993).

Thus, measurements were omitted that fell in the intersection of  $12^\circ$  and  $18^\circ$  in the temporal field and  $2^\circ$  in the superior field and  $6^\circ$  in the inferior field.

## Individual eye models: Optimization

The input wavefront errors were used by Zemax OpticStudio optical design software (version 20.3; Ansys Inc, [www.ansys.com](http://www.ansys.com)) to reverse engineer individual eye models. During this process, parameters of the eye models, such as the spacing (thickness), curvatures, asphericities, tilts, and translations of surfaces, were iteratively searched by the *global hammer optimization* tool in the software.

An error function (*merit function*) was used to constrain each anatomical parameter to within normative ranges of the typical population and to evaluate the ray-traced wavefront error resulting from each combination of parameters (each iteration of each model) by comparing those aberrations with the input wavefront error. Weights were assigned to each parameter in the error function; zero weight meant

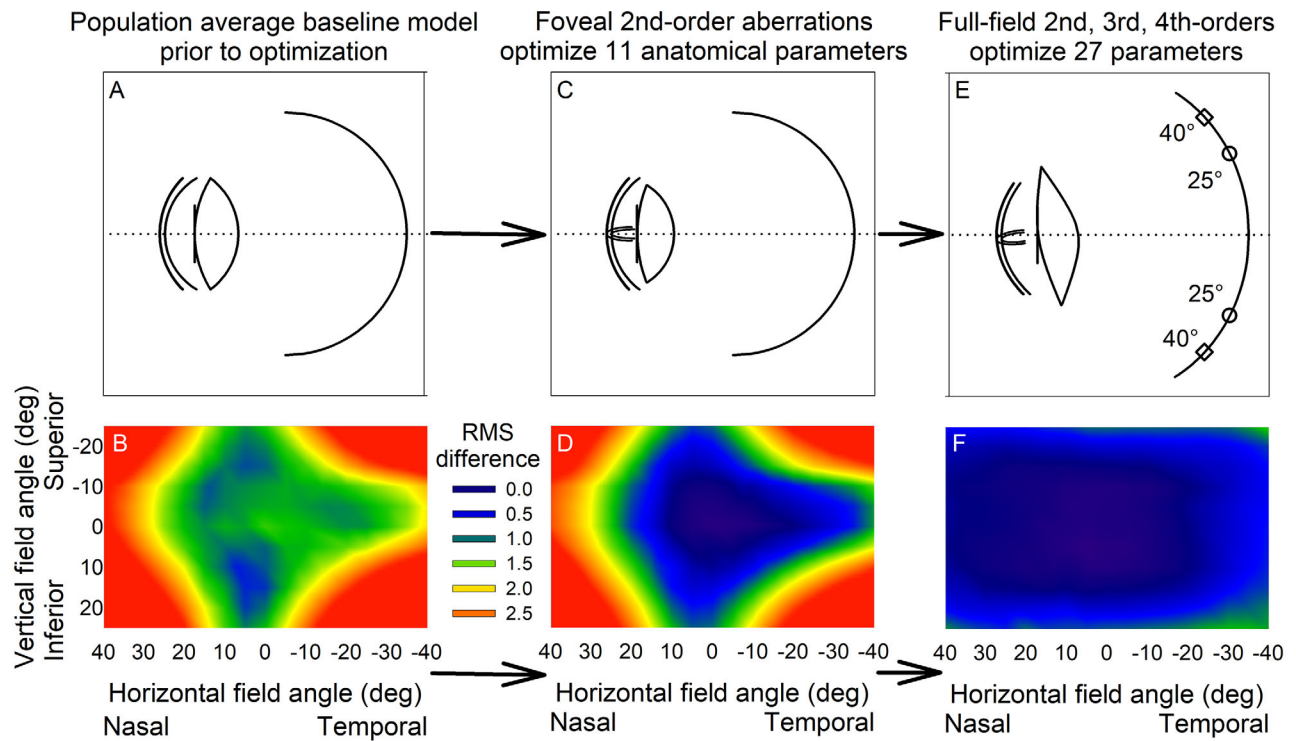


Figure 2. Stages of optimizing and evaluating an individual anatomical eye model. The first row illustrates a section through the models, which increase in complexity from (A) to (C) to (E). Second row (B), (D), (F) shows an example of the total root mean square (RMS) difference between input (measured) and output second-, third-, and fourth-order Zernike aberrations across the field for each stage of the modeling. (A and B) Before optimization, each eye model began with population averages for all anatomical parameters. (C and D) Measured foveal second-order aberrations (defocus and astigmatism) were used to optimize 11 anatomical parameters (Table 1). (E and F) Measured second-, third-, and fourth-order aberrations across the visual field were used to optimize 27 anatomical parameters (Table 1) including positions (thicknesses), curvatures, asphericities, tilts, and decentrations of surfaces.

that the parameter could become any value during optimization, while a large weight penalized the error function if the parameter passed the limits defined for it. The constraints of the anatomical parameters were weighted heavily ( $10^6$ ) to ensure the optimization resulted in anatomically plausible eye models. Lower- and higher-order individual Zernike coefficients were weighted 10 and 1, respectively, which roughly corresponded with their proportional magnitudes across the sample of eyes. This different weighting of lower- and higher-order aberrations also helped to guide the optimization over the field as eccentricity from the fovea increased.

A two-step optimization process was performed (Figure 2) that began with a generic average eye model and an error function that permitted the modification of 11 anatomical variables (Table 1) to optimize only second-order (defocus and astigmatism) foveal aberrations. This first optimization lasted approximately 3 hours and served to streamline the second optimization step by providing a better starting point. During this first step, surface principal meridians were spherical and coaxial along the  $z$ -axis (no tilts

or translations in  $x$  or  $y$  directions were allowed here).

The second optimization step used a more elaborate error function that drove 27 anatomical variables to optimize for all Zernike aberrations in the second, third, and fourth radial orders across all visual field positions. This optimization lasted 5 to 6 days per eye (Intel Xeon Gold 6252N CPU 2.30 GHz; 9.26 GB RAM) and was allowed to run until 6 million anatomical configurations had been evaluated. This process ensured that a minimum error function was reached (many hours without a better combination of parameters being found). Owing to ocular chromatic aberrations (as described in the [Ocular chromatic aberrations](#)), optimizing eye models at one wavelength has the potential that rays at another wavelength might not pass through every element of the model. Thus, the error function for the second optimization step ensured that rays over a  $\pm 40^\circ$  (horizontal)  $\times$   $\pm 25^\circ$  (vertical) object field could be traced through each surface of the model for wavelengths from 400 to 900 nm. This function also ensured that elements did not overlap with each other (e.g., that a shallow anterior chamber

Structure	Parameter	Ideal emmetropic	Typical emmetropic	−2.75 D myopic
Anterior cornea	x Radius of curvature (mm)*	7.686	7.686	7.782
	x Conic Q‡	−0.241	−0.179	−0.355
	y Radius of curvature (mm)*	7.699	7.699	7.811
	y Conic Q‡	−0.231	−0.058	−0.318
Posterior cornea	x Radius of curvature (mm)*	6.527	6.527	6.343
	x Conic Q‡	−0.273	−0.184	−0.228
	y Radius of curvature (mm)*	6.701	6.701	6.712
	y Conic Q‡	−0.204	−0.174	0.171
Total cornea	Central thickness (mm)*	0.587	0.587	0.585
	x Decentration (mm)‡	0.182	0.472	−0.248
	y Decentration (mm)‡	−0.237	−0.600	−0.139
	Rotation about x (deg)‡	−0.883	−2.992	−0.195
	Rotation about y (deg)‡	−2.041	−5.682	2.668
	Rotation about z (deg)*	175.291	175.291	0.754
Aqueous	Central thickness (mm)*†	3.453	3.453	3.430
Anterior lens	Radius of curvature (mm)*†	11.545	11.545	11.072
	Conic Q†‡	−6.282	−2.063	−7.295
Posterior lens	Radius of curvature (mm)*†	−5.456	−5.456	−5.356
	Conic Q†‡	−4.231	−4.707	−3.625
Total lens	Central thickness (mm)*†	3.958	3.958	3.807
	x Decentration (mm)†‡	−0.036	−0.462	−0.088
	y Decentration (mm)†‡	−0.184	−0.510	−0.300
	Rotation about x (deg)†‡	−0.874	−4.618	−2.657
	Rotation about y (deg)†‡	−1.288	−3.121	1.459
Vitreous	Central thickness (mm)*	16.252	16.212	17.344
Retina	Radius of curvature (mm)	−18.634	−18.634	−18.483
	Conic Q‡	0.691	1.019	0.528

Table 1. Anatomical definitions of the *ideal emmetropic*, *typical emmetropic*, and *−2.75 D myopic* Berkeley eye models. *Notes:* These 27 anatomical parameters were allowed to vary in the optical design software during the optimization of the individual (cohort) eye models; the subset of 11 parameters marked with asterisks (\*) were those that varied during the first step of the optimization (Figure 2). Parameters marked with a dagger (†) varied during the accommodation re-optimization (Table 2), and those marked with a double dagger (‡) varied during the optimization of the *typical emmetropic* model (see Methods). Sign conventions and order of translations and rotations are described in the text. References to *x*, *y*, and *z* are the parlance used in the optical design software. Similar anatomical specifications of the individual eyes in each refractive cohort are summarized in the Supplementary Materials.

did not result in a steep posterior cornea touching the anterior lens surface).

Tilts and translations are implemented in the optical design software using a coordinate break before the first surface of an anatomical element (such as the cornea or lens) and a coordinate return after the last surface of the element; because the global coordinate system is always restored, tilts and translation are relative to a common reference axis (what would be the optical axis in a coaxial system). Positive horizontal (*x*) and vertical (*y*) translations were right (temporal for a right eye) and superior, respectively (Figure 1) when viewing from the perspective of the eye. Tilt magnitudes are in degrees of a right-handed convention with respect to the positive axes and the field angles described above. Thus, positive tilt about *x* (tip, pitch) means that the top of the cornea or lens tilts back; positive tilt about *y* (tilt, yaw) involves the right side of an element pivoting forward; tilt about

*z* (roll) is analogous to cylinder axis and opposite in direction—when viewing the eye model from the front (cornea) along the optical axis, positive tilt about *z* is a clockwise rotation.

A tilted and rotated position is arrived at by first translating in *x* and *y*, then rotating about the *x* axis (rotating *y* and *z* axes to new orientations), then about the new *y* axis (which rotates the *x* and *z* axes), and finally about the new *z* axis—this order is achieved by setting the coordinate break order flag to zero in Zemax. Tilts and decentrations are reversed in the opposite order (*z* tilt, *y* tilt, *x* tilt, and *y* and *x* decentrations) by setting the order flag to one at the corresponding coordinate return. This ordering is not relevant to the optimization process and is already set in the supplementary lens design files, but would be necessary if regenerating the eye models in different software.

## Individual eye models: Anatomy

Surfaces and media of the eye models were constrained based on anatomical ranges from literature (Atchison et al., 2005; Dubbelman, Weeber, Van Der Heijde, & Völker-Dieben, 2002, Dubbelman, Van der Heijde, & Weeber, 2005; Faria-Ribeiro et al., 2014; Ortiz, Pérez-Merino, Gamba, de Castro, & Marcos, 2012; Rosales, Dubbelman, Marcos, & van der Heijde, 2006; Rozema, Atchison, & Tassignon, 2011). All elements could effectively translate in the axial ( $z$ ) direction when the thickness of a surface or medium was altered. Across all surfaces, the conic constant  $Q$  convention was used, where  $Q > 0$  is an oblate ellipse,  $Q = 0$  is a circle,  $-1 < Q < 0$  is a prolate ellipse,  $Q = -1$  is parabolic, and  $Q < -1$  is hyperbolic. Refractive indices of all ocular media were dispersive (Navarro, 2014), that is, they mimicked the chromatic aberration of the human eye (Appendix B). Conversion of Cauchy equation coefficients from literature (Atchison & Smith, 2005; Navarro, 2014) to the format used by Zemax (*extended formula*) is included in Appendix C.

The anatomical elements of the models were as follows.

Anterior and posterior corneal surfaces were biconic, which is like a toric surface, but with aspheric principal meridians. Curvatures, asphericities, and separation of both surfaces could be modified by the optical design software. The cornea was allowed to translate in horizontal ( $x$ ) and vertical ( $y$ ) directions and to rotate about all three-dimensional axes.

Anterior to the crystalline lens in the eye models is an iris aperture element that functions as the system stop.

The crystalline lens, defined by Navarro (Navarro, 2014; Navarro, Palos, & González, 2007), consists of aspheric anterior and posterior surfaces and a gradient refractive index (GRIN) that increased monotonically from the edges of the lens toward the center. We adopted two recommended conventions (Navarro, 2014; Navarro et al., 2007): The spatial increment (measured along the  $z$ -axis) in which the refractive index changed was every 0.1 mm, and the highest refractive index was located at 60% of the total lens thickness, that is, slightly posterior to the axial midpoint of the lens.

The optical industry usually defines aberrations over the exit pupil of the system because the beam has a well-defined edge at that location (Applegate et al., 2000). Zemax also uses a reference sphere defined at the exit pupil as the reference for optical path difference computations (Zemax OpticStudio 20.3 User Manual, 2020). Input aberration data used for the optimization of the eye models were defined over pupil diameters of 4 mm across all measured eccentricities.

Mapping from elliptical to round pupils was already performed by the source studies (Jaeken, Lundström, & Artal, 2011a; Liu et al., 2016; Lundström et al., 2009; Mathur et al., 2009; Polans et al., 2015; Pusti et al., 2023)—four methods of wavefront reconstruction over elliptical pupils have been shown similarly accurate with respective reconstruction errors being negligible at the level of numerical computation (Wei & Thibos, 2010). Measurements at larger sizes were scaled down to 4 mm (Schwiegerling, 2002); eyes with pupil diameters of less than 4 mm were excluded. Once the optimization of an eye model was completed, pupil size could be modified and ray tracing performed to provide output aberrations at different pupil sizes, as demonstrated in the **Pupil size and position**. Ray aiming was set to “real” in Zemax, which traces rays over the system stop, which was defined using the “float by stop size” setting.

Retinal curvature and asphericity have been associated with refractive error patterns (Wallman & Winawer, 2004), changes in magnification across the field (Hastings, Banks, & Roorda, 2022), and how retinal image velocities change during eye movements (Rucci & Victor, 2018). The retina was allowed to change curvature and asphericity to best fit the input wavefront error data across the visual field. Because all other surfaces could move in the  $z$ -dimension (by changing thickness), allowing the retina to move axially was redundant. The optimization error function ensured that the retinal shape allowed rays from across the  $\pm 40^\circ$  horizontal  $\times$   $\pm 25^\circ$  vertical field to intersect with this surface—for instance, it prevented the retina from becoming too steeply curved that eccentric rays would miss it.

## Metrics used in results

The output of the optical eye models is described using numerous metrics, most fundamentally using a seventh-order normalized Zernike aberration coefficient expansion fit over the exit pupil of the eye model. Individual Zernike terms are reported when commenting on the expectations of Seidel aberration theory and in one method of calculating dioptric defocus that only used the second-order Zernike defocus term (Equation A4, Appendix D). A combination of rotationally symmetric second-, fourth-, and sixth-order Zernike terms is used in the preferred calculation of dioptric defocus (Equation A3, Appendix D). The metric of relative peripheral defocus was computed for both of these dioptric defocus metrics by subtracting the defocus value at fixation (0,0) from all field locations. Hence, if defocus at fixation is  $-1.00$  D, and at an arbitrary field position ( $x,y$ ) is  $-1.75$  D, relative defocus at fixation is  $0.00$  D and at ( $x,y$ ) is  $-0.75$  D.

Root mean square (RMS) wavefront error is a common single value metric that captures the collective

magnitude of all aberrations; lower values are better, meaning that less aberration is present. Similarly, comparing two wavefront errors is performed here by taking the RMS of the per-term differences in Zernike coefficients of the two wavefront errors. Although it is a common metric, RMS wavefront error does not describe optical quality unambiguously because it does not consider that aberrations interact visually (Hu, Ravikumar, Hastings, & Marsack, 2020) and that different aberrations affect vision uniquely (Applegate,

Sarver, & Khemsara, 2002). The Strehl ratio is a widely used optical metric that is more sensitive to the unique visual effect and interaction of aberrations, and is computed as the ratio of the point spread function of the eye model (under various conditions, such as field location, correction modality, and accommodative state) to the point spread function of an optical system with the same exit pupil size that is limited only by diffraction (Smith, 2000; Thibos et al., 2004). Hence, the Strehl ratio ranges from 0 (worst) to 1 (best).

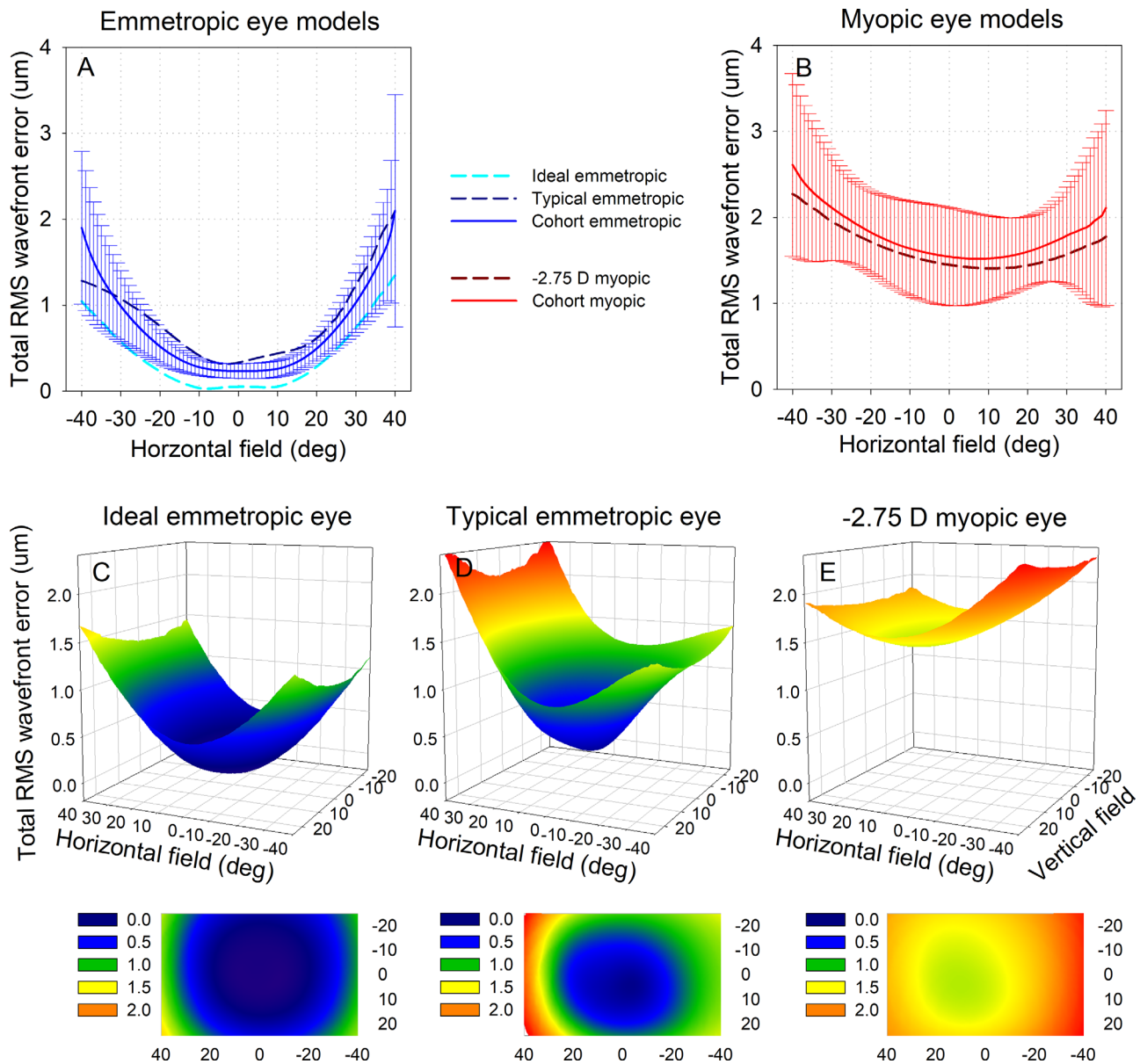


Figure 3. Total root mean square (RMS) wavefront error, where lower values are better, for a 4 mm pupil diameter. (A and B) Sections along the horizontal visual field for (A) emmetropic and (B) myopic eye models. Error bars around the cohort traces are  $\pm 1$  standard deviation. (C, D, and E) Total RMS wavefront error across the  $80^\circ \times 50^\circ$  field of the models. At fixation (zero in the horizontal and vertical fields), the emmetropic eyes have less total aberration than the myopic eyes, predominantly owing to lower-order refractive error. Changes in total aberrations with increasing field angle are generally greater (steeper contour to the plots and surfaces) for the emmetropic models than the myopic models.

## Accommodation

After the eye models were optimized as described, eyes that were also measured under accommodative demand were additionally re-optimized using those accommodated wavefront error data. During this re-optimization process, anatomical parameters of the cornea and retina were kept constant and only 10 parameters that related to accommodation were allowed to vary (Table 1); these parameters included the radii of curvature and conic constants of both lens surfaces, tilts and decentrations of the lens, and thickness (or depths) of the lens and anterior chamber. Total axial length was constrained to be the same as the relaxed eye models. As described [Accommodation](#), not all parameters had a significant contribution to fitting the accommodated wavefront error data and a simpler model of accommodation was found to be satisfactory.

## Defining an average eye model by pooling individual eyes

There are many potential methods of computing average eye models from cohorts of individual eye models; we considered four such methods. First, the 27 resultant anatomical parameters that define each individual eye model after optimization could be averaged. Second, the aberrations output after optimization by each individual eye model could be averaged and used to drive a new single optimization of the 27 anatomical parameters using the same optimization process as was undergone by each individual model. Third, the input aberrations for each eye could be pooled and used for the optimization process. The second and third methods differ in that all eyes contribute aberrations to all field points in the second method because the output of the models are continuous and can be sampled at any increment, whereas the field positions at which the input aberrations were measured differed across studies.

As will be shown either averaging the aberrations or averaging the anatomical parameters of eyes in the emmetropic cohort results in an eye model of optical quality that is far superior to that of the individual eyes. This is because many aberrations (Porter, Guirao, Cox, & Williams, 2001) and many anatomical parameters (below) average close to zero. The *ideal emmetropic* eye model presented in the Results is such a model and used the first method described—anatomical parameters were averaged to define the model. This model is intended for applications that currently use schematic or paraxial eye models with minimal amounts of typical aberrations.

A fourth approach was used to generate the *typical emmetropic* eye model in this work. Optimization began from the anatomical average *ideal emmetropic* model.

Anatomical parameters that had the same sign across all eyes in the emmetropic cohort and, therefore, could be averaged, were not permitted to change from the average values—these included radii of curvatures and thicknesses (Table 1). Anatomical parameters that were distributed around zero (included both positive and negative values) across the individual eyes were set as variable and, again, constrained within anatomical limits—these parameters included tilts, decentrations, and conic constants. This model was then optimized using an error function (*merit function*) that drove RMS at each field point to be the median RMS value of the individual eyes at each field point. Unlike many aberrations that are distributed around zero and average close to zero, RMS is always positive and, hence, the median value of the emmetropic cohort could be used.

The myopic cohort spanned a larger range of refractive errors than the emmetropic cohort and resulted in anatomical parameters than could be averaged to produce a single representative eye model (Figure 3 and Table 1).

## Results and discussion

The outputs of the individual and representative anatomical eye model parameters are presented first, then those models are used to illustrate total aberrations and image quality across the field, followed by examinations of specific aberration terms, relative peripheral defocus, and ocular chromatic aberrations. Thereafter, some clinical applications of the models are illustrated. Although an emphasis of this work is the wide-field results, all eye models also need to be applicable to foveal vision, thus, foveal results are also described, including quality control comparisons of the eye models with established literature.

### Individual eye models

Ultimately, wavefront error measurements from 28 emmetropic and 20 myopic individual eyes satisfied all criteria for inclusion. After the optimizations, all anatomical parameters of the resultant eye models were verified individually to have remained within the normative limits from the literature that were constrained by the error function, and they are thus individually plausible biometric parameters. However, population covariances between all anatomical parameters are not sufficiently understood in literature to assert whether the total combined anatomy of each eye model is plausible.

In agreement with literature (Atchison et al., 2005), most of the eye models had an oblate shape ( $Q > 0$ )

over the  $\pm 40^\circ$  horizontal  $\times$   $\pm 25^\circ$  vertical extent of visual field optimized by the software.

The two cohorts of individual emmetropic and myopic eye models are used in this work to generate means and standard deviations of the reported outputs (aberrations and metrics) for each refractive group. After the optimization of all individual eye models was completed, anatomical parameters of all left eyes were mirrored about the vertical to be like right eyes. These combined parameters were used to define the *ideal emmetropic*, *typical emmetropic*, and  $-2.75$  D myopic eye models described in the Methods and presented in Table 1. The anatomical parameters of the individual eye models are summarized in the Supplementary Materials. Zemax designs for all individual (cohort) and representative eye models also accompany the paper as Supplementary Materials.

## RMS aberration outputs of the eye models

The primary output of the optical eye models is wavefront error described using Zernike aberration coefficients over a visual field extent of  $\pm 40^\circ$  horizontally  $\times$   $\pm 25^\circ$  vertically. Because the refracting surfaces and media of the models are continuous, aberrations can be extracted at any desired increment within that field;  $1^\circ$  rectangular increments are generally used for the data that follow unless otherwise stated.

RMS wavefront error of the refractive cohorts and *ideal emmetropic*, *typical emmetropic*, and  $-2.75$  D myopic eye models are shown in Figure 3. At fixation (0,0), the emmetropic eyes have less total aberration than the myopic eyes, predominantly owing to the contribution of lower-order refractive error. However, the relative change in total aberrations with increasing field angle is greater for the emmetropic models (steeper curvatures of the surfaces in Figures 3A, C, and D) than the myopic models (flatter plots in Figures 3B and E).

Across all individual emmetropic eyes, the mean  $\pm$  standard deviation location of the best (lowest) RMS wavefront error output in the field was at  $-3.2^\circ \pm 6.4^\circ$  in the temporal field and  $0.8^\circ \pm 9.2^\circ$  in the inferior field, which was similar to the best locations of the input data of  $1.2^\circ \pm 9.8^\circ$  and  $2.6^\circ \pm 7.4^\circ$ , respectively. The mean  $\pm$  standard deviation total RMS wavefront error difference between the input and output aberrations across all eyes at the fovea was  $0.135 \pm 0.039$   $\mu\text{m}$  and across all eyes and all field locations was  $0.263 \pm 0.079$   $\mu\text{m}$ , which compared well with  $0.2$   $\mu\text{m}$  (Goncharov, Nowakowski, Sheehan, & Dainty, 2008) and  $0.23 \pm 0.09$   $\mu\text{m}$  (Liu & Thibos, 2019) from the literature, where optimization was performed over smaller fields. Further, although the 6 million iterations of the 27 variables provided a good agreement of the input and

output aberrations, they were not identical, as would be expected if the models were overfit.

Predicted foveal high-contrast logMAR visual acuity (Watson & Ahumada, 2008) for the emmetropic cohort was  $-0.19 \pm 0.08$ , which is comparable with the normative acuity of young eyes from literature (Elliott, Yang, & Whitaker, 1995).

Across all emmetropic eyes, the RMS wavefront error patterns shown in Figures 3A, C, and D are representative of most individual emmetropic eye models in the sample, where the aberration magnitude is lowest near fixation and increases essentially monotonically with increasing eccentricity. This progression corresponds with the Strehl ratio patterns in Figure 4, where best optical quality is found centrally and decreases essentially monotonically away from fixation.

In Figure 3A, note how averaging the 27 anatomical parameters of the emmetropic cohort (*ideal emmetropic*) results in aberrations far superior (lower magnitude) than the individual eyes in the cohort; the *typical emmetropic* model represents the cohort much more realistically. These aberration patterns correspond to Strehl ratio patterns where the *ideal emmetropic* eye (Figure 4A) has considerably better optical quality than both the *typical emmetropic* model (Figure 4B) and the cohort of emmetropic eyes (Figure 4C). The Strehl ratio is particularly sensitive to defocus, where  $0.25$  D (which is within the definition of emmetropia) causes more than a log unit decrease in the metric (Hastings, Applegate, et al., 2022).

Similar to RMS wavefront error, the mean  $\pm$  standard deviation location of the best (highest) Strehl ratio output was  $-3.2^\circ \pm 7.0^\circ$  in the temporal field and  $0.1^\circ \pm 11.1^\circ$  in the inferior field, which was near to the best locations of the input data  $-0.5^\circ \pm 9.1^\circ$  and  $0.0^\circ \pm 8.5^\circ$ , respectively. If we take (0,0) in our  $xy$  coordinate system as corresponding with fixation (line of sight) (Applegate et al., 2000), this means that best optical quality is located in the direction of the conventional ocular optical axis (Nowakowski, Sheehan, Neal, & Goncharov, 2012) relative to the line of sight.

The uncorrected myopic models are defocused considerably at the fovea and across the field, such that the Strehl ratio is so low that it is meaningless (Smith, 2000). Therefore, myopic models are discussed further when correction modalities are compared.

## Individual aberrations

Because the output of wavefront error at every field location is described by Zernike aberration coefficients, the change in individual aberrations can be examined over the field. This is illustrated in Figure 5 using the *ideal emmetropic* and *typical emmetropic* eye models.

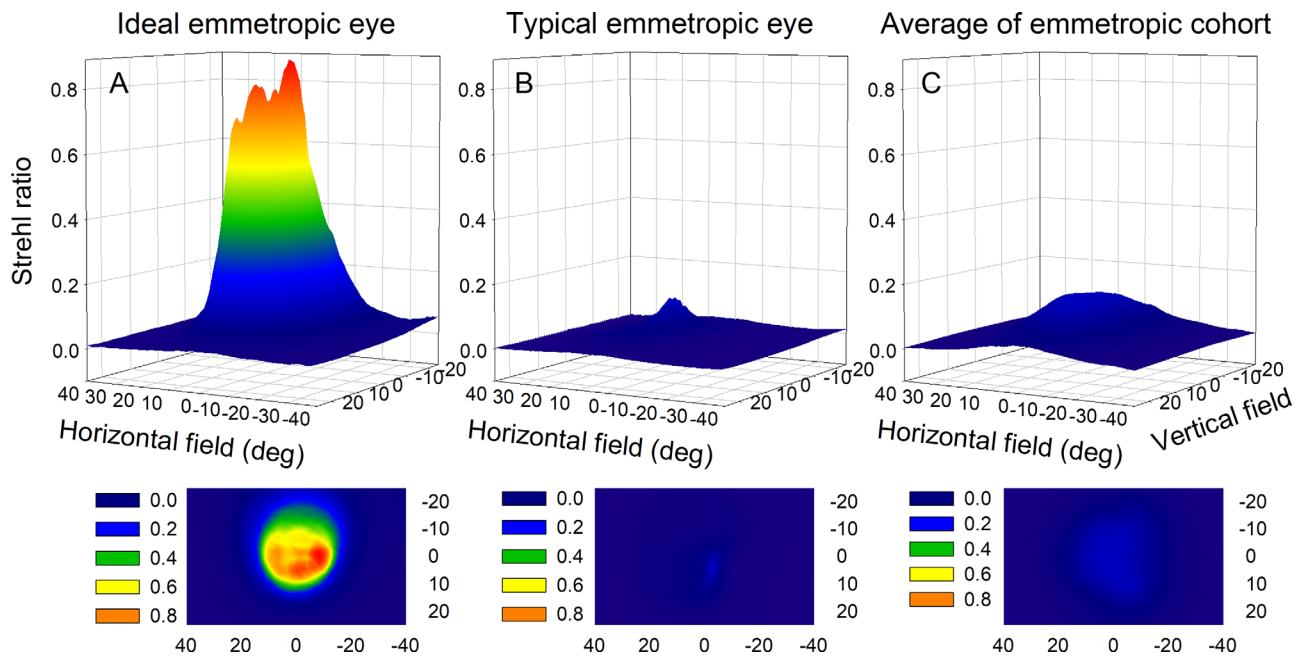


Figure 4. Strehl ratio, where larger values mean better optical quality, across the  $80^\circ \times 50^\circ$  field for (A) the *ideal emmetropic* model, (B) the *typical emmetropic* eye model, and (C) the pooled average of all 28 eyes in the emmetropic cohort. Across all models best optical quality is found centrally and decreases essentially monotonically away from fixation. The excellent optical quality of the *ideal emmetropic* eye relative to the typical and individual models is obvious. Uncorrected myopic eye models (not shown) are considerably defocused at the fovea and across the field, which results in low and meaningless Strehl ratios (Smith, 2000). These myopic models are discussed again when ophthalmic correction modalities are illustrated.

Individual aberration terms generally changed with field angle as predicted from Seidel aberration theory (Atchison & Smith, 2023; Mathur, Atchison, & Scott, 2008; Mazzaferri & Navarro, 2012). The magnitudes of second-order astigmatism (Figure 5A) and third-order coma (Figure 5B) increased with field eccentricity in quadratic and linear fashions, respectively, while fourth-order spherical aberration (Figure 5C) is relatively constant, only becoming slightly more positive with eccentricity. Small deviations from these predictions, and the differences between the *ideal emmetropic* and *typical emmetropic* eye models, are due to our modeling using aspheric surfaces, as well as allowing tilts and decentrations of optical elements.

## Relative peripheral defocus

Defocus and relative peripheral defocus as functions of field angle are commonly reported when studying the onset and progression of ametropias, such as myopia, as well as the design of interventions for its remediation (Lundström et al., 2009; Smith et al., 2009). It is important to recall that both the location of the optical image shell and retinal shape determine relative peripheral defocus as shown in Figure 6A. For example,

image shell (Figure 6c) is peripherally hyperopic relative to retina (Figure 6b), but is peripherally myopic relative to retina (Figure 6d), and is foveally emmetropic for both retinas in Figure 6A. Also note that peripheral myopia between (Figure 6c) and (Figure 6d) first increases and then decreases as field angle increases primarily owing to the oblate profile of retina (Figure 6d). This pattern is seen in Figures 6B and C, which illustrate two methods that the eye models from this work could be applied. Curves labeled as cohort are the mean  $\pm$  standard deviation of the cohort of all individual eyes in each of the emmetropic or myopic groups, while curves labeled as ideal, typical, and  $-2.75$  D are the output of the *ideal emmetropic*, *typical emmetropic*, and  $-2.75$  D *myopic* eye models, respectively.

Relative peripheral defocus (in diopters) is commonly plotted in one dimension as a function of horizontal field angle, which is commonly obtained from autorefractometry (Walline et al., 2020) or retinoscopy (Smith et al., 2009). Figures 6B and C show equivalent one-dimensional data and compare two methods of computing diopters from Zernike-defined wavefront error (Thibos et al., 2004); one method only uses the second-order Zernike defocus term, whereas the second method uses rotationally symmetric second-, fourth-, and sixth-order Zernikes (Appendix D). The computed

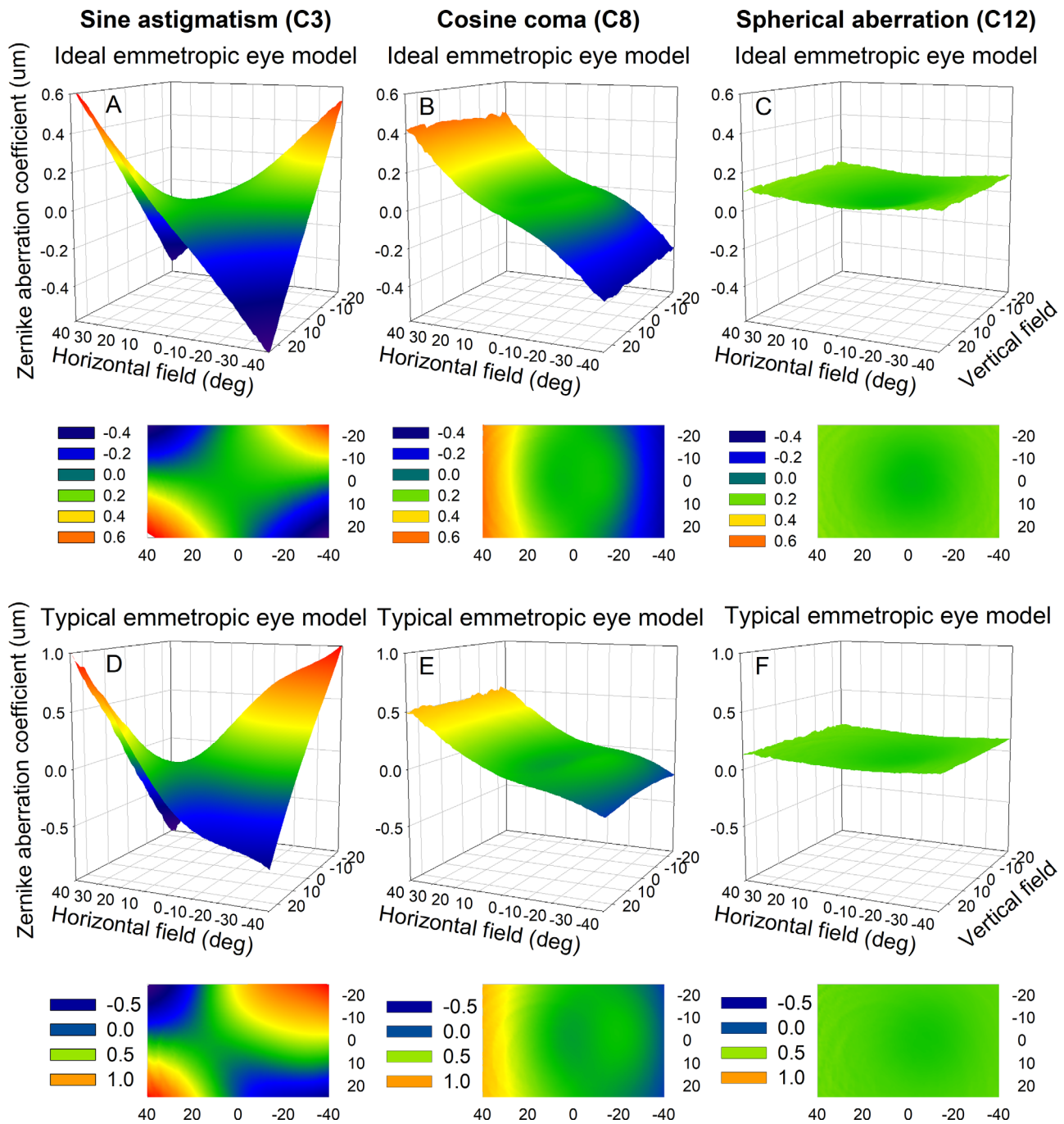
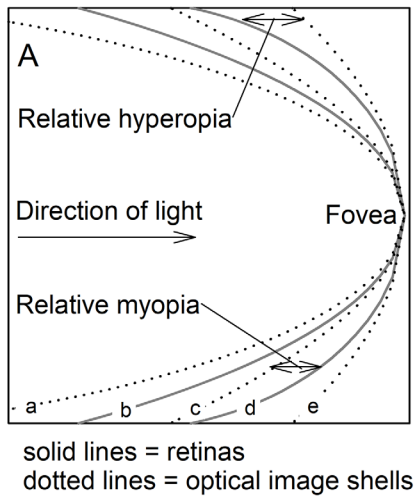


Figure 5. Individual Zernike aberration terms of the *ideal emmetropic* and *typical emmetropic* eye models as function of visual field angle for a 4 mm pupil diameter. Increase in the magnitudes of (A and D) second-order astigmatism (Zernike sine term C3 shown), (B and E) third-order coma (Zernike cosine term C8 shown), and (C and F) fourth-order spherical aberration (Zernike term C12) were approximately quadratic, linear, and constant with field angle, respectively. Small deviations from (A and D) quadratic, (B and E) linear, and (C and F) constant behaviors predicted by Seidel aberration theory are due to our modeling using aspheric surfaces and allowing tilts and decentrations of optical elements.

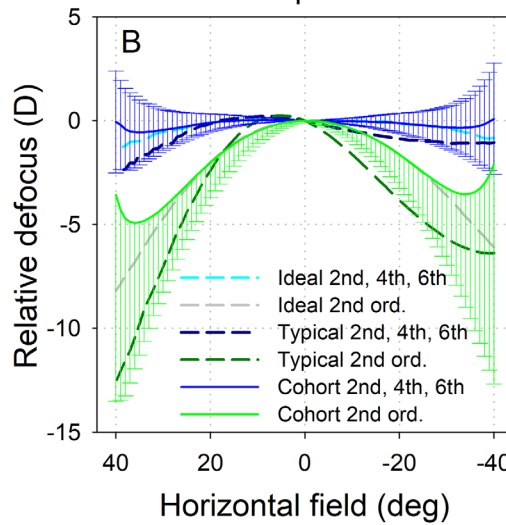
diopters are considerably larger in magnitude when only the second-order Zernike defocus term is used. The large standard deviation error bars in the peripheral fields are due to different retinal shapes—note that only the lower error bars are plotted for the second-order calculation. The interaction of defocus with spherical

aberrations is well-known (Thibos, Bradley, Liu, & López-Gil, 2013), and all subsequent plots of relative peripheral defocus use the second calculation (incorporating rotationally symmetric second- through sixth-order Zernike terms). Moreover, subjective refractive error is relatively consistent as a function of

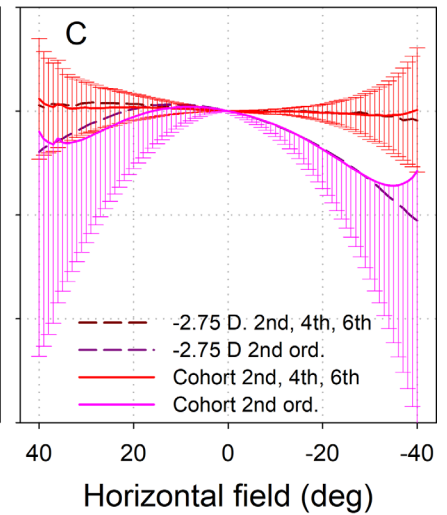
Two retinas, three image shells



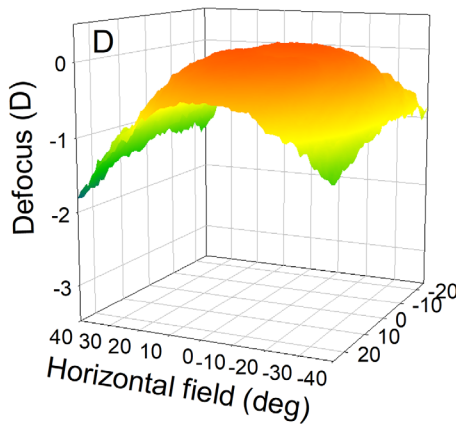
Emmetropic models



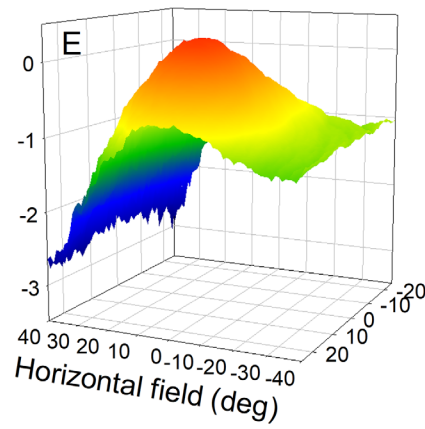
Myopic models



Ideal emmetropic eye



Typical emmetropic eye



-2.75 D myopic eye

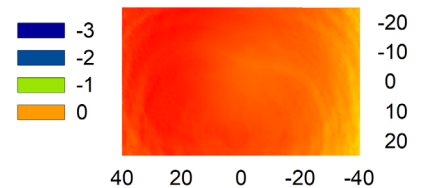
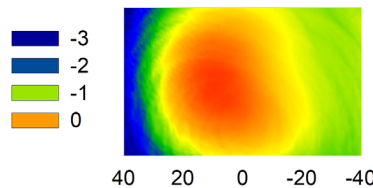
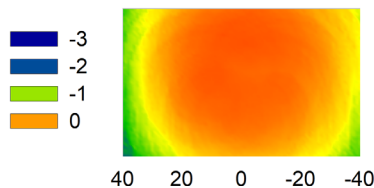
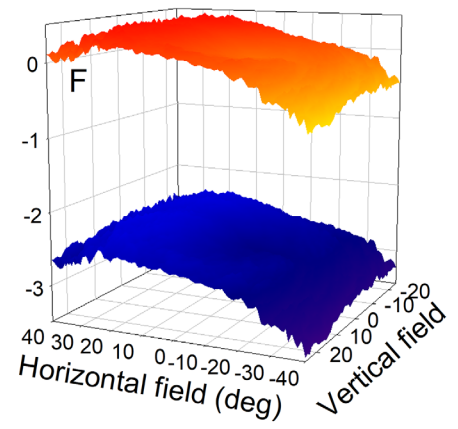


Figure 6. Defocus and relative defocus for a 4 mm pupil diameter. (A) The relative locations of the hypothetical optical image shells (a, c, e) and retinal shapes (b, d) determine relative peripheral defocus. Image shell (c) is foveally emmetropic for both retinas (b) and (d), but is peripherally hyperopic relative to retina (b) and peripherally myopic relative to retina (d). Relative peripheral myopia between (c) and (d) first increases, then decreases, with field angle primarily owing to the oblate profile of retina (d). This is the reason for the recoiling patterns in the far periphery of the cohort curves in (B) and (C). (B and C) Relative peripheral defocus along the horizontal field meridian calculated using either second-order or second-, fourth-, and sixth-order Zernikes (Appendix D); (E and F) use the latter calculation. (D and E) Relative peripheral defocus is essentially the same as actual defocus for the *ideal emmetropic* and *typical emmetropic* models because foveal dioptric defocus is +0.005 D and -0.023 D, respectively. (F) Relative (upper) and actual (lower) defocus surfaces for the -2.75 D myopic eye model are offset from each other by 2.761 D of foveal myopic defocus. Like total root mean square wavefront error in Figure 3, the relative change in defocus with field angle is greater (steeper plots and surfaces) for emmetropic eye models than for the myopic model.

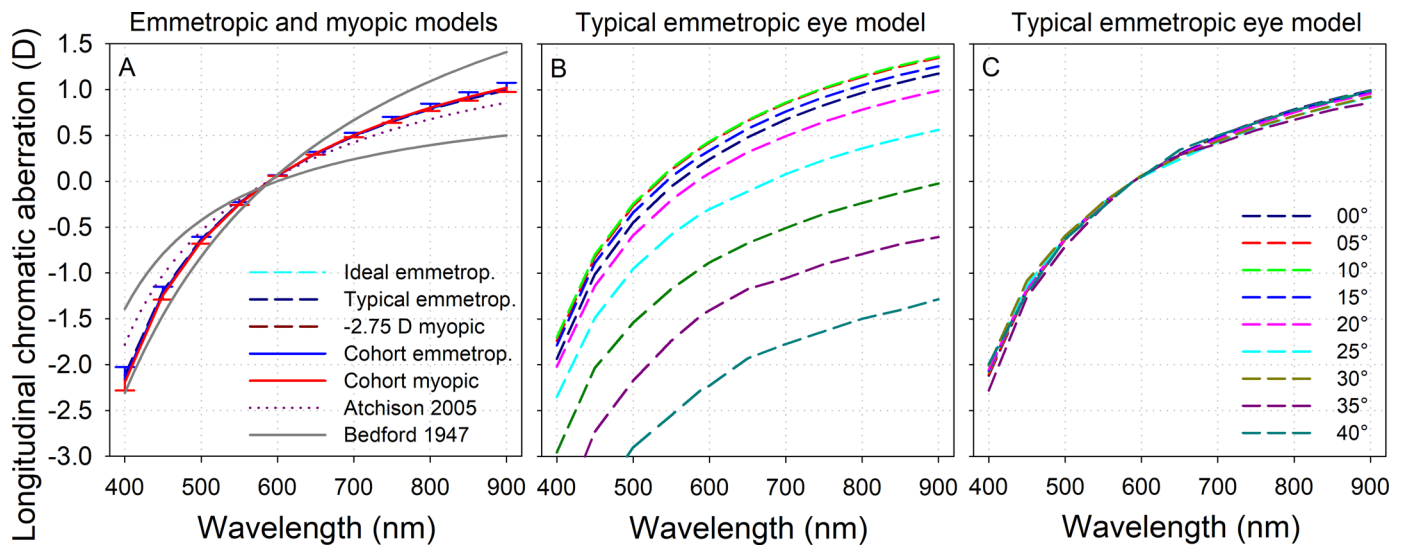


Figure 7. Foveal and peripheral longitudinal chromatic aberration (LCA) (D) calculated using second-, fourth- and sixth-order Zernikes (Appendix D). (A) Foveal LCA of all emmetropic and myopic eye models fell within typical ranges (Bedford & Wyszecki, 1957) and near to a population model (Atchison & Smith, 2005). Error bars are 1 standard deviation. (B) Dioptric differences as a function of wavelength for fixation and eight locations in the nasal horizontal field of the *typical emmetropic* model; legend for (B) is as in (C). In (B), curves for eccentricities 0° through 15° coincide and the vertical offset of the other curves is primarily owing to relative peripheral defocus described above. (C) Subtracting the foveal defocus value of a curve at 589 nm from all values in that curve (relative peripheral defocus) shows that relative LCA is consistent as a function of field angle.

pupil size (Charman, Jennings, & Whitefoot, 1978) and, as shown in the section on pupil size, the inclusion of fourth- and sixth-order spherical aberrations results in much more consistent refractive behavior across pupil sizes than when only using the second-order Zernike term.

The optical eye models can provide defocus and relative peripheral defocus continuously in two field dimensions, as in Figures 6D, E, and F. Only the relative defocus surface is shown (Figures 6D and E) because foveal dioptric error is +0.005 D and −0.023 D for the *ideal emmetropic* and *typical emmetropic* models, respectively, meaning that relative and absolute defocus surfaces are essentially identical.

Relative and absolute defocus surfaces are shown separately for the uncorrected average myopic eye model (Figure 6F); these are offset from each other by the foveal dioptric defocus amount of −2.761 D. Like the total RMS wavefront error surfaces in Figure 3, the relative change in defocus with field angle is faster (steeper plot surfaces) for the emmetropic eye models (Figures 6D and E) than for the myopic model (Figure 6F). In agreement with much of the input data, the emmetropic models generally have a greater occurrence of relative peripheral myopia across the field, while the uncorrected myopic models have a mixture of relative peripheral myopia and hyperopia. Relative peripheral defocus is also illustrated later below for the −2.75 D myopic eye model wearing ophthalmic corrections.

## Ocular chromatic aberrations

### Foveal and peripheral longitudinal chromatic aberration (LCA)

LCA is the axial variation in focus as a function of wavelength, where shorter wavelengths refract more and focus anterior (more myopically or less hyperopically) relative to longer wavelengths, which refract less and focus more posteriorly. This concept is applicable along any field angle. Dioptric values for LCA were calculated using second-, fourth-, and sixth-order Zernike terms (Appendix D).

The literature contains relatively consistent characterizations of foveal LCA. All present eye models fell within typical ranges (Bedford & Wyszecki, 1957) and agreed well with a population model (Atchison & Smith, 2005) of foveal LCA (Figure 7A). Figure 7B shows LCA curves for nine eccentricities as a function of wavelength. The same data are plotted in Figure 7C after relative peripheral defocus is taken into account and reveals that relative axial dioptric differences in focus owing to wavelength are generally consistent across the field. This was done by subtracting the foveal defocus values at a nominal wavelength—here 589 nm is used—from all dioptric values at each field position (each curve), which results in all curves intersecting at (589, 0). Literature (Jaeken, Lundström, & Artal, 2011b), using only a second-order computation of diopters, has found a similarly

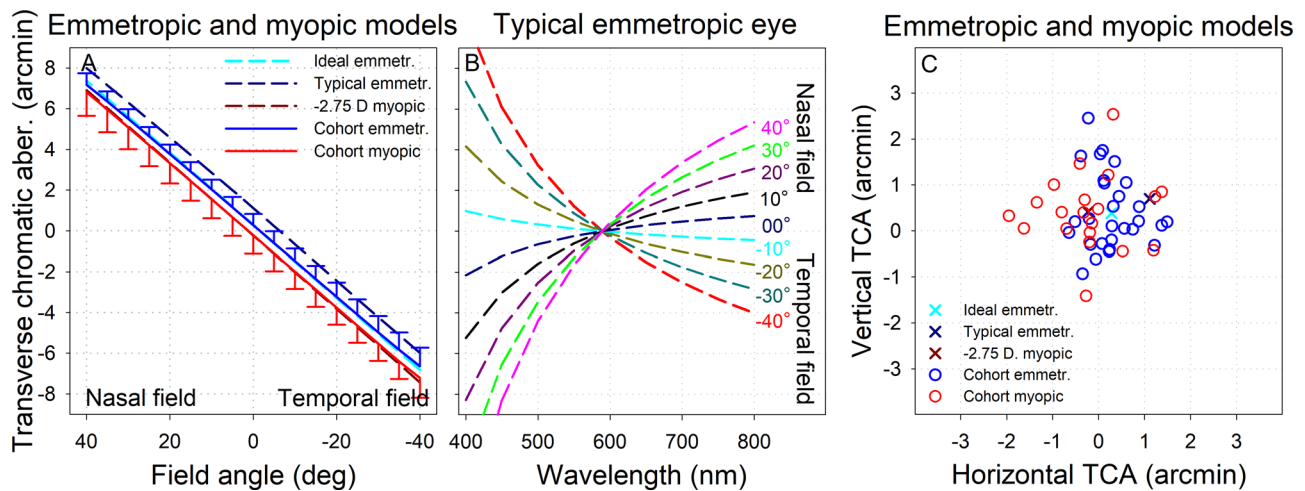


Figure 8. Transverse chromatic aberration (TCA), where positive horizontal and vertical TCA mean that shorter wavelengths are more nasal and inferior on the retina than longer wavelengths, respectively. (A) TCA between 842 and 543 nm increases in magnitude with increasing field angle away from the fovea. (B) General model of TCA: optical models are not limited to discrete wavelengths. Each curve shows a different eccentricity, where the TCA between any wavelengths at any eccentricity can be calculated. (C) Foveal TCA between 842 and 543 nm for all individual and representative eye models.

small change in LCA with eccentricity as function of (approximately) horizontal field position out to 30° from fixation.

### Foveal and peripheral transverse chromatic aberration (TCA)

TCA is the difference in the retinal image size and location as a function of wavelength, and sometimes is called chromatic difference in magnification. The literature typically reports TCA as the visual angle difference (minutes of arc) between two wavelengths referenced to the center of the entrance pupil (Ogboso & Bedell, 1987; Winter et al., 2016). The location of the optical entrance pupil changes slightly with wavelength—but by less than 0.004 mm over the wavelength range used here (400–900 nm). Computation of TCA for each eye model began with the points where the chief rays of each given wavelength intersected with the retina. These ray heights at the retinal surface were converted to arcminutes via trigonometry using the entrance pupil position for 555 nm and Equation 1, from Suheimat, Zhu, Lambert, and Atchison (2016), where a sign in the denominator is modified to calculate the  $z$ -coordinate of the retinal intersection point.

$$z = \frac{x^2}{r - \sqrt{r^2 - (1 + Q)x^2}}, \quad (1)$$

where  $x$  is the ray height on the retina in millimeters,  $r$  is the retinal radius of curvature in millimeters and

negative in sign, and  $Q$  is the conic constant of the retina.

Figure 8A shows TCA in a common manner as the difference between 842 and 543 nm. Positive TCA values for a right eye mean that, for polychromatic light from a field location, shorter wavelengths fall more nasally on the retina than longer wavelengths; this pattern was also consistent across four measured eyes (Winter et al., 2016).

Optical modeling software is not limited to only discrete wavelengths that are typically filtered from projectors (Ogboso & Bedell, 1987) or super-continuum lasers (Winter et al., 2016). Figure 8B shows a generalization of TCA (in arcmin) using the horizontal field meridian of the average emmetropic eye model. Each curve relates to a different eccentricity, where the relationships between any wavelengths at any of the eccentricities can be calculated.

Figure 8C plots foveal TCA between 842 and 543 nm for all individual and representative eye models. Magnitudes of foveal TCA are comparable with literature, despite small differences in the wavelengths used (Roorda et al., 2023; Rynders, Lidkea, Chisholm, & Thibos, 1995).

### Pupil size and position

Eye models permit the simulation of perturbations in pupil size and position—two examples are shown in Figure 9. As mentioned in the section on relative defocus, subjective refractive error is relatively consistent as a function of pupil size (Charman et al., 1978) and the models behave similarly. With a 1-mm

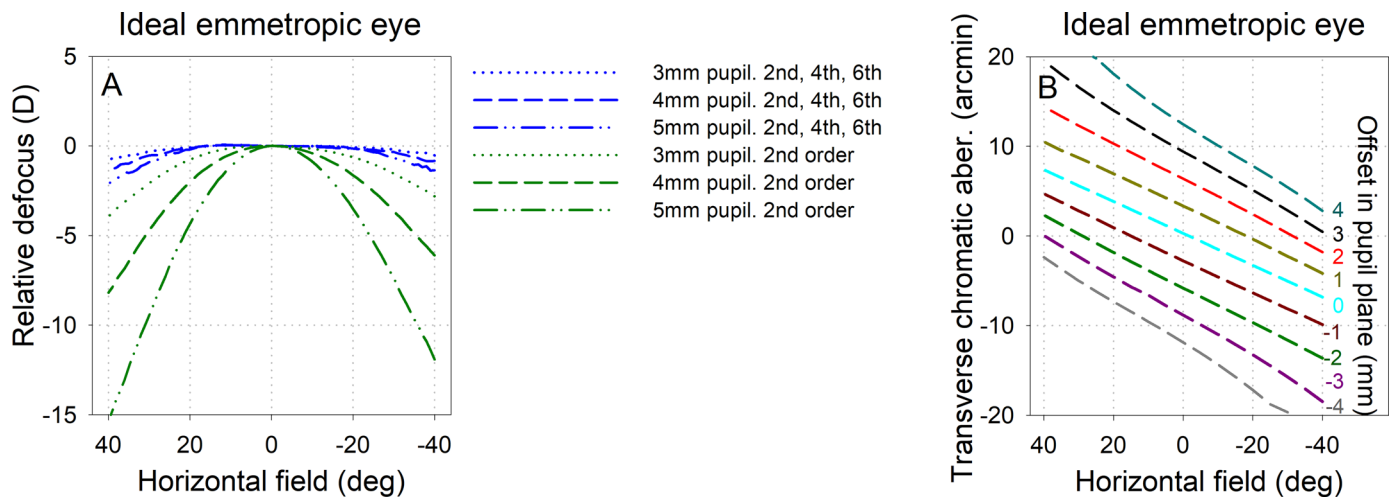


Figure 9. The effects of changing pupil size and position. (A) The inclusion of fourth- and sixth-order spherical aberrations, results in much more consistent refractive behavior across pupil sizes (Charman et al., 1978) than when only using the second-order Zernike term. (B) Predicted changes in transverse chromatic aberration that could result from a misalignment of the effective 4-mm diameter pupil, such as due to an improperly positioned corneal inlay or a misaligned projected psychophysical stimulus beam. The zero-offset curve is the same as the corresponding one in Figure 8A between 842 and 543 nm. Other curves are for horizontal offsets in the effective pupil position ranging from  $-4$  mm to  $+4$  mm, where negative offsets mean nasal offsets of the pupil relative to eye.

change in pupil diameter in either direction from 4 mm, to 3 mm and 5 mm, foveal dioptric defocus (using second-, fourth-, and sixth-order rotationally symmetric Zernike terms) changed by less than 0.03 D. Note that these computations use ray tracing through the surfaces and media of the models rather than algebraic scaling of Zernike coefficients with pupil size, where the same dioptric conversion would be expected a priori. Figure 9A also emphasizes how the inclusion of fourth- and sixth-order spherical aberrations results in much more consistent refractive behavior across pupil sizes than when only using the second-order Zernike term.

The eye models can also be used to predict changes in TCA that could result from an effective misalignment of the pupil (Figure 9B), such as if a corneal inlay was positioned improperly or if a projected psychophysical stimulus was misaligned with the measurement beam for correcting aberrations in an adaptive optics system. These are equivalent to changes measured by simulating an offset pupil (Thibos, Bradley, Still, Zhang, & Howarth, 1990; Ye, Bradley, Thibos, & Zhang, 1991). The zero-offset curve in Figure 9B is the same as the corresponding one in Figure 8A between 842 and 543 nm. The other curves are for horizontal offsets in the effective pupil position ranging from  $-4$  mm to  $+4$  mm, where negative offsets mean that the iris aperture in the model, which is immediately anterior to the lens and serves as the stop in the system was nasally offset from the  $z$ -axis (optical axis in a rotationally symmetric system) (Figure 1). Real ray aiming was kept on for this analysis.

## Accommodation

### Anatomical results of accommodation

Of the 48 individual eye models, 32 had accompanying wavefront error measured under accommodative demand and these were re-optimized using a subset of 10 anatomical parameters (Table 1), while the total axial length was constrained to match that of the relaxed model. Only six of the parameters had significant contributions to the accommodative response (Figure 10), namely, anterior lens radius of curvature and conic constant, posterior lens radius of curvature and conic constant, anterior chamber depth, and central lens thickness. Because, like previous accommodating models (Liu & Thibos, 2019; Schwiegerling, 2004), any thickening of the lens was accompanied by a commensurate decrease in aqueous chamber depth, only five of those anatomical parameters were independent. The mean change in these parameters as a function of accommodative demand are included in Table 2 and are compared with models from the literature in Figure 10. The four parameters that did not contribute significantly to accommodation were decentrations along, and rotations around, the horizontal and vertical axes. Mean changes in these parameters per diopter as functions of accommodative demand were less than 0.001 mm, 0.002 mm,  $0.213^\circ$ , and  $0.062^\circ$  respectively.

After optimization, the mean  $\pm$  standard deviation RMS wavefront error difference between input and

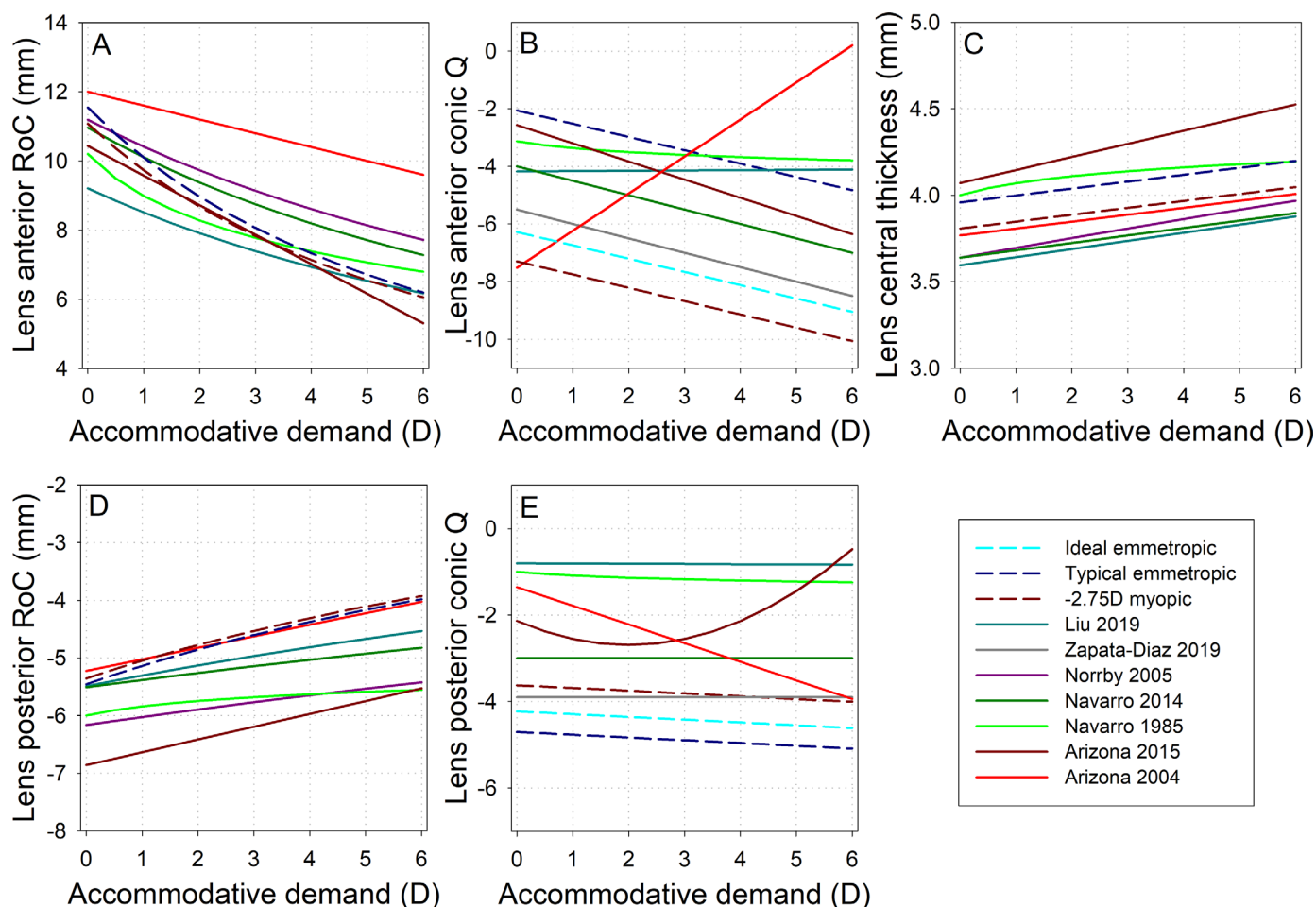


Figure 10. Change in anatomical parameters with accommodation for the *ideal emmetropic*, *typical emmetropic*, and *-2.75 D myopic* eye models. Numerical definitions of these relationships are in Table 2, which result from re-optimization of all Zernikes across all field positions. Thickening of the lens during accommodation was accompanied by a commensurate reduction in aqueous chamber depth; only the former is plotted. Parameters for seven accommodating models from literature are also shown; two versions of the Navarro and Arizona models are each included because the earlier versions maintain popularity and are still widely used.

Structure	Parameter	Accommodation change
Aqueous	Central thickness (mm)	Baseline - (0.04*Acc)
Anterior lens	Radius of curvature (mm)	$1/((1/\text{baseline}) + (0.0125*\text{Acc}))$
	Conic Q	baseline - (0.462*Acc)
Posterior lens	Radius of curvature (mm)	$1/((1/\text{baseline}) - (0.0113*\text{Acc}))$
	Conic Q	baseline - (0.064*Acc)
Total lens	Central thickness (mm)	Baseline + (0.04*Acc)

Table 2. Changes in the six anatomical parameters that significantly contributed to the accommodation response of input eyes additionally measures under accommodative demand. *Notes:* Changes are defined as a function of accommodative demand (Acc) in diopters; baseline refers to the relaxed (zero accommodative demand) value of the parameter (Table 1 and Supplementary Materials).

output accommodation aberrations across all field positions and across all eyes was  $0.280 \pm 0.112 \mu\text{m}$ . This finding is understandably a larger difference than resulted from the relaxed eye optimization, because fewer parameters were allowed to vary.

**Optical results of accommodation**

The optical behavior of the eye models during accommodation is also in general agreement with literature. Data in Figure 11 were generated using a flat object at a distance of  $[1/\text{accommodative demand (D)}]$

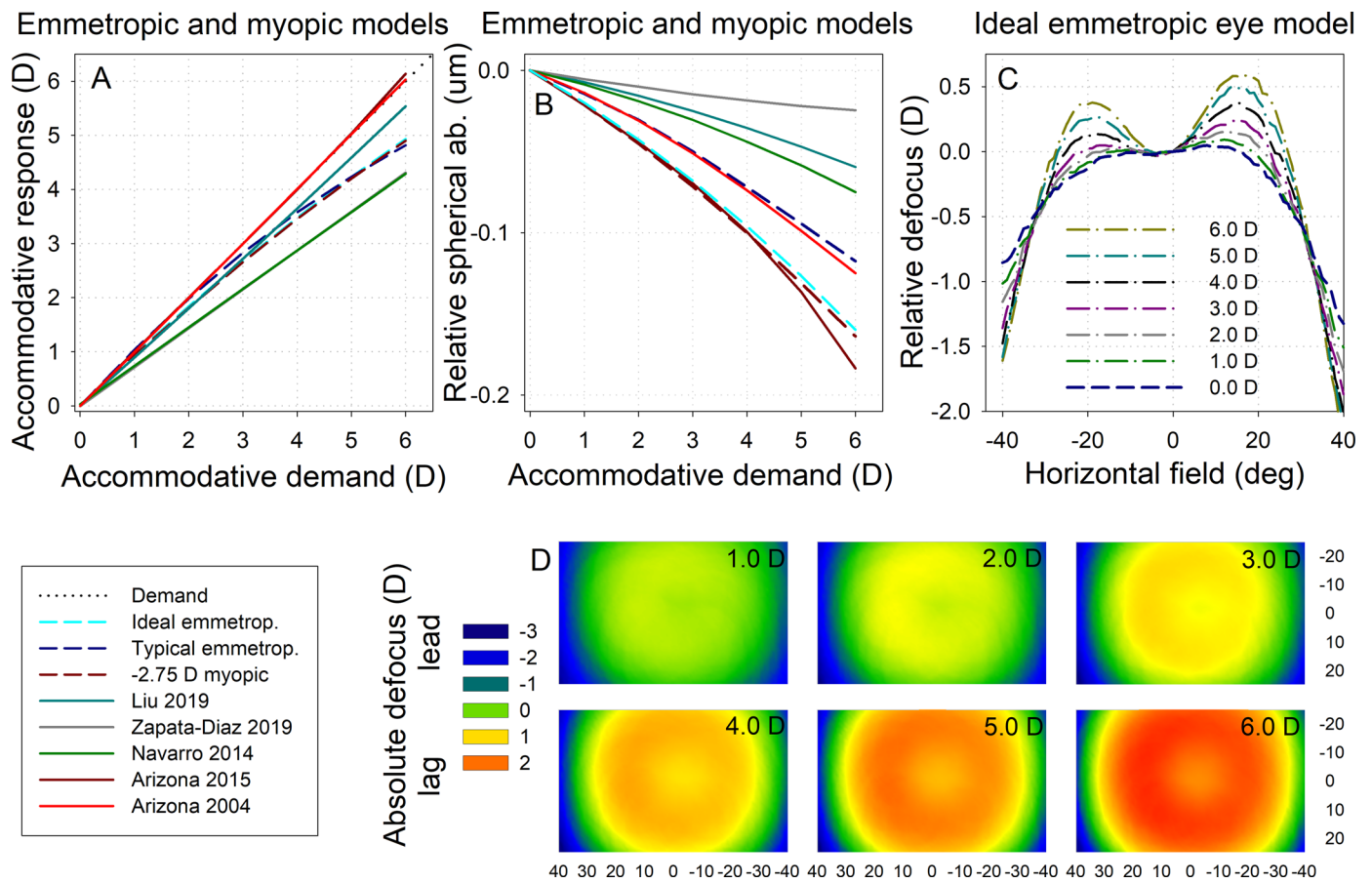


Figure 11. Optical results of accommodation. (A) Accommodative responses (relative to the distance vision dioptric error) at the fovea for demands between 0 and 6 D. Lags or leads are the differences between a plot and the demand (unity) line. Lags are positive differences, leads are negative. The legend for (A) and (B) is below (A). (B) Zernike spherical aberration (C12) becomes relatively more negative with accommodation, in agreement with literature. (C) Relative peripheral defocus across the horizontal field meridian removes the foveal lag of accommodation and reveals peripheral hyperopia with increasing accommodation. Demands are labeled in the legend. (D) Actual accommodation (not relative as in [C]) across the field for all demands. All objects were flat surfaces at  $1/\text{demand}$  from the cornea.

from the cornea. Accommodative response is typically evaluated at the fovea rather than peripherally; here the response of the models is accurate at low demands and begins to lag as demand increases; for all three models (*ideal emmetropic*, *typical emmetropic*, and *-2.75 D myopic*), the lag is approximately 1 D at a 6 D demand (Figure 11A).

Responses of other accommodating models from literature are mixed: The response of the two Arizona models (Schwiegerling, 2004, 2018) accurately matches all demands, whereas some other models (Navarro, 2014; Zapata-Díaz, Radhakrishnan, Charman, & López-Gil, 2019) show considerable lags. The responses of the present models are between these two extremes. The Liu 2019 model was based on Table 2 of Liu and Thibos (Liu & Thibos, 2019). The Zapata-Díaz 2019 (Zapata-Díaz et al., 2019) curve was based on their Equation 6A, which was essentially identical to data extracted from Figure 10 of Navarro (Navarro, 2014) for the Navarro, 2014 curve.

Figure 11B shows the change in spherical aberration (Zernike C12) as a function of accommodative demand. Data were generated or extracted as per Figure 11A except for the Zapata-Díaz 2019 curve (from their Figure 3A; Zapata-Díaz et al., 2019) and the Navarro 2014 curve (from their Figure 11; Navarro, 2014). Slopes of linear fits to measured changes in spherical aberration as a function of accommodative demand vary from  $-0.01 \mu\text{m}/\text{D}$  (Lopez-Gil et al., 2008) to approximately  $-0.04 \mu\text{m}/\text{D}$  (Cheng et al., 2004).

Computing relative peripheral defocus (Figure 11C) as a function of accommodative demand removes the foveal lag. These relative patterns reveal small amounts of relative hyperopic defocus with increasing accommodation. Figure 11D extends the actual accommodation (not relative accommodation as in Figure 11C) results from the horizontal field meridian across the full two-dimensional field for six accommodative demands.

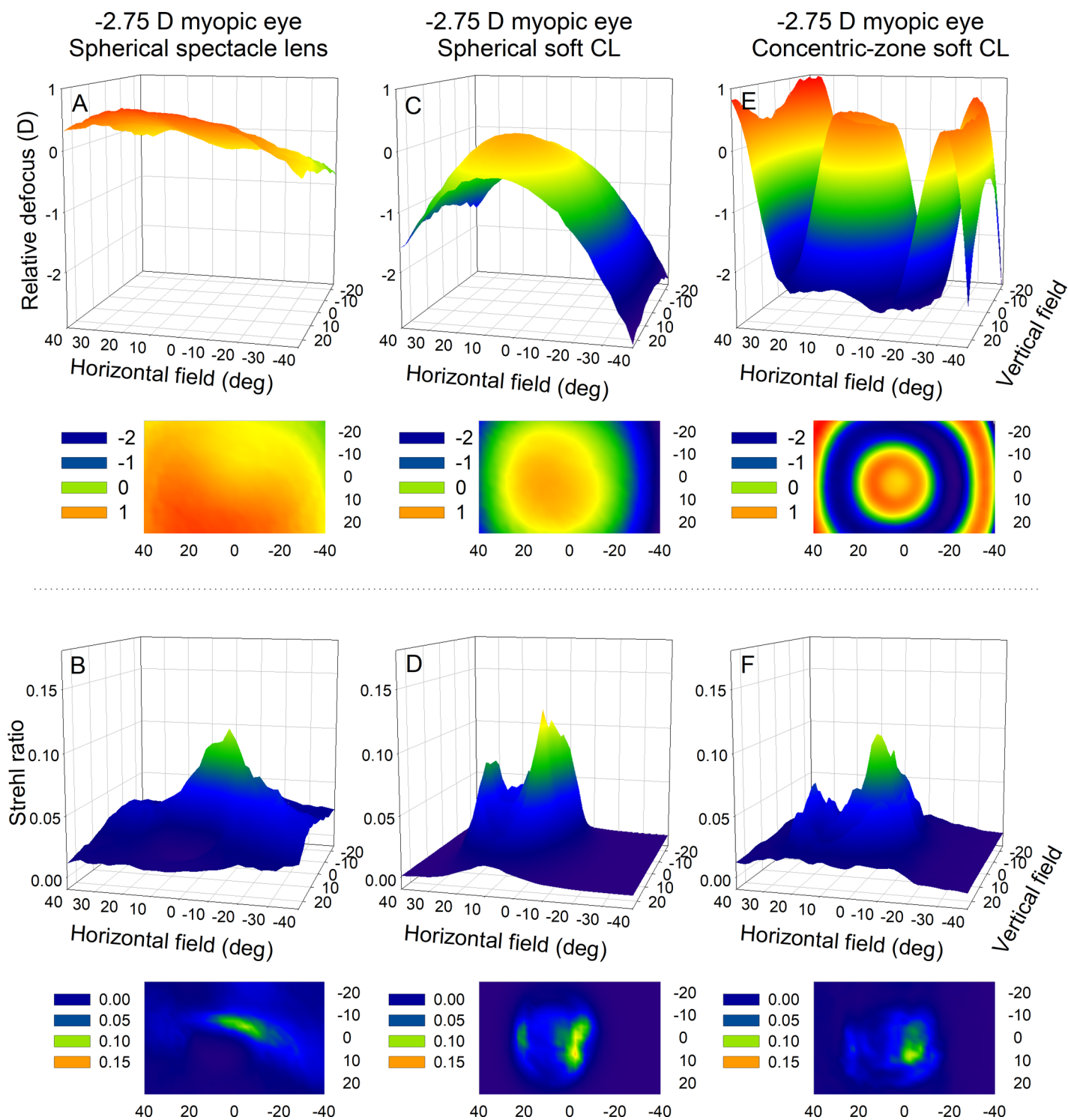


Figure 12. Using the  $-2.75\text{ D}$  myopic eye model to demonstrate ophthalmic corrections for a 4-mm pupil diameter. Relative peripheral defocus (A, C, and E) and the Strehl ratio (B, D, and F) across the visual field for three correction modalities. (A and B) Polycarbonate spectacle lens following a commercial design (SOMO optical, 2022). (C and D) Spherical soft contact lens. (E and F) Concentric zone soft contact lens (Anstice & Phillips, 2011). Both contact lenses aligned with the corneal tilt orientations (Table 1). Relative peripheral defocus for the uncorrected  $-2.75\text{ D}$  myopic eye is shown in Figure 6.

## Example application

### Comparing ophthalmic correction modalities

To demonstrate a hypothetical application of eye models, the  $-2.75$  D myopic eye model was corrected using three ophthalmic modalities: a spherical spectacle lens, a spherical soft contact lens, and a concentric-zone soft contact lens designed to impart relative peripheral myopic defocus. Relative peripheral defocus and the Strehl ratio across the visual field are shown for the three corrections in Figure 12; recall that uncorrected relative peripheral defocus was illustrated for this model in Figure 6.

The spectacle lens was modeled at a 12-mm vertex distance between the posterior spectacle surface and anterior corneal surface, using polycarbonate material (nominal refractive index of 1.586), and was based on a commercial design (SOMO Optical, 2022). The lens center thickness was 1.4 mm and the lens was positioned with  $8^\circ$  pantoscopic tilt and a corresponding 4-mm inferior offset (Brooks & Borish, 2007). It is trivial to modify the surfaces of the spectacle correction to evaluate designs ranging from the least sophisticated planoconcave trial lens to modern aspheric and free-form designs; the selected design is representative of a typical ophthalmic spectacle lens design.

Both contact lenses were modeled as aligning with the corneal tilt orientations and as having a central lens thickness of 0.1 mm and a postlens tear layer central thickness of 0.01 mm (Lin, Graham, Polse, Mandell, & McNamara, 1999). The anterior surface of the spherical contact lens was optimized to minimize foveal dioptric error. Figure 12C shows considerably more peripheral myopic defocus with this contact lens than the spectacle lens.

The concentric multizone soft contact lens designed for myopia control followed the design described by Anstice and Phillips (2011), which is the basis for the MiSight lens (CooperVision Inc, Pleasanton, CA) according to Chamberlain et al. (2019). As illustrated by Anstice and Phillips (2011), the lens consists of five concentric zones, where zones 1 (center), 3, and 5 contain the distance myopic correction, and zones 2 and 4 produced 2 D of myopic retinal defocus—these were implemented in Zemax using the multi-zone-asphere user-defined surface. The pattern of relative peripheral defocus across the field can be seen in Figure 12E.

## Limitations and conclusions

Every modeling effort requires balancing concessions. Here, for instance, both corneal surfaces were modeled as biconic and the whole cornea was allowed to translate and rotate in three-dimensions. Although this aspect of the model was more customizable than rotationally

symmetric and/or coaxial corneal models, elsewhere, the cornea has been modeled as a contour defined by multiple Zernike terms (Navarro, 2014; Rozema, Rodriguez, Navarro, & Tassignon, 2016). Likewise, the crystalline lens surfaces have been characterized in greater detail (Martínez-Enríquez et al., 2023). Adding many additional degrees of freedom would have added to the already lengthy duration of the optimization.

The approach taken here was to optimize each individual eye and use the anatomical output parameters to derive the *ideal emmetropic* eye model. This approach was preferred over reverse-engineering the average model from average Zernike input aberrations (approaches 2 and 3 described in the Methods). Approach 2 (using the output aberrations of the cohorts) resulted in optical quality even better than the *ideal emmetropic* model, and approach 3 (using the input aberrations) resulted in a model with unrealistic microperturbations in aberrations across the field because the input data were sampled at different field increments.

The presented eye models are forward direction models, meaning that rays are traced from object space outside the eye through the refracting surfaces and media in an anterior (cornea) to posterior (retina) direction. In ophthalmic wavefront sensing a beacon point source is generated on the retina and light travels in a reverse direction from posterior to anterior. Unfortunately, there are two obstacles encountered when attempting to optimize a reverse model in Zemax. First, the input wavefront errors were measured across the visual field at angle increments defined in object space outside the eye. The path of a ray from that field point through all the refracting surfaces and media of the eye model, and the ultimate intersection point of that ray with the retina, are both unknown at the onset of the output of the optimization process. Zemax defines a field angle between the object and the entrance pupil, which means that, in a reverse model, the location of the retinal image (the object in a reverse model) would need to be known at the onset for all field points. This would clearly require making numerous undesirable anatomical and optical assumptions. Second, it is desirable to define the object rather than making the object parameters variable. Owing to the considerable variability in retinal shapes of individuals (Atchison et al., 2005; Faria-Ribeiro et al., 2014), we wanted to allow retinal curvatures and asphericities to vary during optimization. In a reverse model, this process would require the object (retina) to have multiple variable degrees of freedom.

These challenges have been encountered in literature where concessions were made of deciding a fixed retinal shape for optimization and estimating the retinal position corresponding to an object space field position. A drawback of this necessity of using a forward model is a difference between the entrance pupil size over

which aberrations were measured and the exit pupil size over which they were output iteratively by the optimization algorithm, with the former being slightly larger than the latter and, for equivalent coefficient values, the output being slightly better optical quality than the input.

Physiological pupil size decreases during accommodation (Kasthurirangan & Glasser, 2005). This behavior is not incorporated automatically by the models because the input wavefront error data collection followed the recommendation of comparing aberrations at a standardized pupil sizes (American National Standards Institute, 2004). Nevertheless, the aberrations used to optimize the anatomical parameters associated with accommodation were measured through physiological pupil sizes (Liu et al., 2016; Lundström et al., 2009; Mathur et al., 2009) and only scaled down (Schwiegerling, 2002) to 4 mm for optimization. Although the models were optimized using wavefront error for a 4-mm pupil, aberrations can be output from the models for many pupil sizes, as was done in Figure 9—and behaved in agreement with literature. That being said, the models have not been overtly validated against pupil sizes other than 4 mm.

Zemax archive files and an Excel summary of all 50 eye models from this work are provided as Supplementary Material. These include the laid-out designs of all models and supporting files, such as those required for the dispersive definition of the ocular media. The individual eye models allow cohorts of emmetropic and myopic eyes to be iteratively modeled in a manner that provides the mean and variability of each cohort. The *ideal emmetropic*, *typical emmetropic*, and  $-2.75 D$  *myopic* eye models defined from each cohort provide representative monochromatic and chromatic aberrations for their cohorts across a  $\pm 40^\circ \times \pm 25^\circ$  extent of visual field that have applications in studying and modeling accommodation, mobility, driving, and mitigating the onset and progression of ametropias.

*Keywords:* eye model, aberration, emmetropic, myopic, peripheral defocus

## Acknowledgments

The authors thank David Atchison for technical discussions and Martin Banks for technical discussions and for suggesting Figure 9B. G.D.H. was funded entirely by membership fees paid to the Center for Innovation in Vision and Optics by member companies. The authors are very grateful to Pablo Artal, David Atchison, Tao Liu, Linda Lundström, Ankit Mathur, Rafael Navarro, James Polans, Dibyendu Pusti, Larry Thibos, and Geunyoung Yoon for generously sharing data with us.

Commercial relationships: none.

Corresponding author: Gareth D. Hastings.

Emails: gdhastings1@gmail.com;

gdhastings@berkeley.edu.

Address: 485 Minor Hall, Herbert Wertheim School of Optometry and Vision Science, University of California Berkeley, Berkeley, CA 94720-2020, USA.

## References

- Akram, M., Baraas, R., & Baskaran, K. (2018). Improved wide-field emmetropic human eye model based on ocular wavefront measurements and geometry-independent gradient index lens. *Journal of the Optical Society of America A*, 35(11), 1954, <https://doi.org/10.1364/JOSAA.35.001954>.
- American National Standards Institute. (2004). *American National Standard for Ophthalmics: Methods for reporting optical aberrations of eyes, ANSI Z80.28–2004*. Merrifield, VA: Optical Laboratory Association.
- Anstice, N., & Phillips, J. (2011). Effect of dual-focus soft contact lens wear on axial myopia progression in children. *Ophthalmology*, 118(6), 1152–1161, <https://doi.org/10.1016/j.ophtha.2010.10.035>.
- Applegate, R., Sarver, E., & Khemsara, V. (2002). Are all aberrations equal? *Journal of Refractive Surgery*, 18(5), s556–s562.
- Applegate, R., Thibos, L., Bradley, A., Marcos, S., Roorda, A., Salmon, T., . . . Atchison, D. (2000). Reference axis selection: Subcommittee report of the OSA working group to establish standards for measurement and reporting of optical aberrations of the eye. *Journal of Refractive Surgery*, 16(5), S656–S658, <https://doi.org/10.3928/1081-597X-20000901-35>.
- Armaly, M. (1969). The size and location of the normal blind spot. *Archives of Ophthalmology*, 81(2), 192–201, <https://doi.org/10.1001/archophth.1969.00990010194009>.
- Atchison, D., Pritchard, N., Schmid, K., Scott, D., Jones, C., & Pope, J. (2005). Shape of the retinal surface in emmetropia and myopia. *Investigative Ophthalmology and Visual Science*, 46(8), 2698–2707, <https://doi.org/10.1167/iops.04-1506>.
- Atchison, D., Scott, D., & Charman, W. (2007). Measuring ocular aberrations in the peripheral visual field using Hartmann-Shack aberrometry. *Journal of the Optical Society of America A, Optics, Image Science, and Vision*, 24(9), 2963–2973, <https://doi.org/10.1364/JOSAA.24.002963>.
- Atchison, D., & Smith, G. (2005). Chromatic dispersions of the ocular media of human eyes. *Journal of the Optical Society of America A*,

- Optics, Image Science, and Vision*, 22(1), 29, <https://doi.org/10.1364/JOSAA.22.000029>.
- Atchison, D., & Smith, G. (2023). *Optics of the human eye* (2nd ed.). CRC Press.
- Atchison, D., & Thibos, L. (2016). Optical models of the human eye. *Clinical and Experimental Optometry*, 99(2), 99–106, <https://doi.org/10.1111/cxo.12352>.
- Bedford, R., & Wyszecki, G. (1957). Axial chromatic aberration of the human eye. *Journal of the Optical Society of America*, 47(6), 564–565, [https://doi.org/10.1364/JOSA.47.0564\\_1](https://doi.org/10.1364/JOSA.47.0564_1).
- Bowrey, H., Zeng, G., Tse, D., Leotta, A., Wu, Y., To, C., ... McFadden, S. (2017). The effect of spectacle lenses containing peripheral defocus on refractive error and horizontal eye shape in the guinea pig. *Investigative Ophthalmology and Visual Science*, 58(5), 2705–2717, <https://doi.org/10.1167/iovs.16-20240>.
- Brooks, C., & Borish, I. M. (2007). *System for ophthalmic dispensing* (3rd ed). Butterworth Heinemann.
- Chamberlain, P., Peixoto-de-Matos, S., Logan, N., Ngo, C., Jones, D., & Young, G. (2019). A 3-year randomized clinical trial of MiSight lenses for myopia control. *Optometry and Vision Science*, 96(8), 556–567, <https://doi.org/10.1097/OPX.0000000000001410>.
- Charman, W., Jennings, J., & Whitefoot, H. (1978). The refraction of the eye in the relation to spherical aberration and pupil size. *British Journal of Physiological Optics*, 32, 78–93.
- Cheng, H., Barnett, J., Vilupuru, A., Marsack, J., Kasthurirangan, S., Applegate, R., ... Roorda, A. (2004). A population study on changes in wave aberrations with accommodation. *Journal of Vision*, 4(4), 272–280, <https://doi.org/10.1167/4.4.3>.
- Dubbelman, M., Van der Heijde, G., & Weeber, H. (2005). Change in shape of the aging human crystalline lens with accommodation. *Vision Research*, 45(1), 117–132, <https://doi.org/10.1016/j.visres.2004.07.032>.
- Dubbelman, M., Weeber, H., Van Der Heijde, R., & Völker-Dieben, H. (2002). Radius and asphericity of the posterior corneal surface determined by corrected Scheimpflug photography. *Acta Ophthalmologica Scandinavica*, 80(4), 379–383, <https://doi.org/10.1034/j.1600-0420.2002.800406.x>.
- Elliott, D., Yang, K., & Whitaker, D. (1995). Visual acuity changes throughout adulthood in normal, healthy eyes: Seeing beyond 6/6. *Optometry and Vision Science*, 72(3), 186–191.
- Faria-Ribeiro, M., López-Gil, N., Navarro, R., Lopes-Ferreira, D., Jorge, J., & González-Méjome, J. (2014). Computing retinal contour from optical biometry. *Optometry and Vision Science*, 91(4), 430–436, <https://doi.org/10.1097/OPX.0000000000000225>.
- Fernández, E., & Artal, P. (2008). Ocular aberrations up to the infrared range: From 632.8 to 1070 nm. *Optics Express*, 16(26), 21199–21208.
- Goncharov, A., Nowakowski, M., Sheehan, M., & Dainty, C. (2008). Reconstruction of the optical system of the human eye with reverse ray-tracing. *Optics Express*, 16(3), 1692–1703, <https://doi.org/10.1364/OE.16.001692>.
- Hastings, G., Applegate, R., Schill, A., Hu, C., Coates, D., & Marsack, J. (2022). Clinical applications of personalising the neural components of visual image quality metrics for individual eyes. *Ophthalmic and Physiological Optics*, 42(2), 272–282, <https://doi.org/10.1111/opo.12937>.
- Hastings, G., Banks, M., & Roorda, A. (2022). Radial and tangential retinal magnifications as functions of visual field angle across spherical, oblate, and prolate retinal profiles. *Translational Vision Science Technology*, 11(9), 10:1–17, <https://doi.org/10.1167/tvst.11.9.10>.
- Hu, C., Ravikumar, A., Hastings, G., & Marsack, J. (2020). Visual interaction of 2nd to 5th order Zernike aberration terms with vertical coma. *Ophthalmic and Physiological Optics*, 40, 669–679, <https://doi.org/10.1111/opo.12718>.
- Jaeken, B., Lundström, L., & Artal, P. (2011a). Fast scanning peripheral wave-front sensor for the human eye. *Optics Express*, 19(8), 7903, <https://doi.org/10.1364/OE.19.007903>.
- Jaeken, B., Lundström, L., & Artal, P. (2011b). Peripheral aberrations in the human eye for different wavelengths: Off-axis chromatic aberration. *Journal of the Optical Society of America A, Optics, Image Science, and Vision*, 28(9), 1871–1879, <https://doi.org/10.1364/JOSAA.28.001871>.
- Jung, H., Ghosh, A., & Yoon, G. (2015). Measurements of peripheral ocular aberrations under natural viewing conditions. *Investigative Ophthalmology and Visual Science*, 56(7), 1725.
- Kang, P., Gifford, P., & Swarbrick, H. (2013). Can manipulation of orthokeratology lens parameters modify peripheral refraction? *Optometry and Vision Science*, 90(11), 1237–1248, <https://doi.org/10.1097/OPX.0000000000000064>.
- Kasthurirangan, S., & Glasser, A. (2005). Characteristics of pupil responses during far-to-near and near-to-far accommodation. *Ophthalmic and Physiological Optics*, 25(4), 328–339, <https://doi.org/10.1111/j.1475-1313.2005.00293.x>.
- Labhishetty, V., Cholewiak, S., & Banks, M. (2019). Contributions of foveal and non-

- foveal retina to the human eye's focusing response. *Journal of Vision*, 19(12), 1–15, <https://doi.org/doi.org/10.1167/19.12.18>.
- Lin, M., Graham, A., Polse, K., Mandell, R., & McNamara, N. (1999). Measurement of post-lens tear thickness. *Investigative Ophthalmology and Visual Science*, 40(12), 2833–2839.
- Liu, T., Sreenivasan, V., & Thibos, L. (2016). Uniformity of accommodation across the visual field. *Journal of Vision*, 16(3), 6, <https://doi.org/10.1167/16.3.6>.
- Liu, T., & Thibos, L. (2019). Customized models of ocular aberrations across the visual field during accommodation. *Journal of Vision*, 19(9), 13, <https://doi.org/10.1167/19.9.13>.
- Llorente, L., Diaz-Santana, L., Lara-Saucedo, D., & Marcos, S. (2003). Aberrations of the human eye in visible and near infrared illumination. *Optometry and Vision Science*, 80(1), 26–35.
- Lopez-Gil, N., Fernandez-Sanchez, V., Legras, R., Montes-Mico, R., Lara, F., & Nguyen-Khoa, J. (2008). Accommodation-related changes in monochromatic aberrations of the human eye as a function of age. *Investigative Ophthalmology and Visual Science*, 49(4), 1736, <https://doi.org/10.1167/iovs.06-0802>.
- Lundström, L., Gustafsson, J., & Unsbo, P. (2009). Population distribution of wavefront aberrations in the peripheral human eye. *Journal of the Optical Society of America A, Optics, Image Science, and Vision*, 26(10), 2192–2198, <https://doi.org/10.1364/JOSAA.26.002192>.
- Lundström, L., Mira-Agudelo, A., & Artal, P. (2009). Peripheral optical errors and their change with accommodation differ between emmetropic and myopic eyes. *Journal of Vision*, 9(6), 1–11, <https://doi.org/10.1167/9.6.17>.
- Marcos, S., Martínez-Enriquez, E., Vinas, M., de Castro, A., Dorronsoro, C., Bang, S., ... Artal, P. (2021). Simulating outcomes of cataract surgery: important advances in ophthalmology. *Annual Review of Biomedical Engineering*, 23(1), 277–306, <https://doi.org/10.1146/annurev-bioeng-082420-035827>.
- Martínez-Enríquez, E., Curatolo, A., de Castro, A., Birkenfeld, J., González, A. M., Mohamed, A., ... Marcos, S. (2023). Estimation of the full shape of the crystalline lens in-vivo from OCT images using eigenlenses. *Biomed Optics Express*, 14(2), 608, <https://doi.org/10.1364/BOE.477557>.
- Mathur, A., Atchison, D., & Charman, W. (2009). Effect of accommodation on peripheral ocular aberrations. *Journal of Vision*, 9(12), 20–20, <https://doi.org/10.1167/9.12.20>.
- Mathur, A., Atchison, D., & Scott, D. (2008). Ocular aberrations in the peripheral visual field. *Optics Letters*, 33(8), 863–865, <https://doi.org/10.1364/OL.33.000863>.
- Mazzaferri, J., & Navarro, R. (2012). Wide two-dimensional field laser ray-tracing aberrometer. *Journal of Vision*, 12(2), 1–14, <https://doi.org/10.1167/12.2.2>.
- Mira-Agudelo, A., Lundström, L., & Artal, P. (2009). Temporal dynamics of ocular aberrations: Monocular vs binocular vision. *Ophthalmic and Physiological Optics*, 29(3), 256–263, <https://doi.org/10.1111/j.1475-1313.2009.00655.x>.
- Mozaffari, S., LaRocca, F., Jaedicke, V., Tiruveedhula, P., & Roorda, A. (2020). Wide-vergence, multi-spectral adaptive optics scanning laser ophthalmoscope with diffraction-limited illumination and collection. *Biomedical Optics Express*, 11(3), 1617–1632, <https://doi.org/10.1364/BOE.384229>.
- Nam, J., Rubinstein, J., & Thibos, L. (2010). Wavelength adjustment using an eye model from aberrometry data. *Journal of the Optical Society of America A*, 27(7), 1561–1574.
- Navarro, R. (2014). Adaptive model of the aging emmetropic eye and its changes with accommodation. *Journal of Vision*, 14(13), 21–21, <https://doi.org/10.1167/14.13.21>.
- Navarro, R., Palos, F., & González, L. (2007). Adaptive model of the gradient index of the human lens I formulation and model of aging ex vivo lenses. *Journal of the Optical Society of America A*, 24(8), 2175, <https://doi.org/10.1364/JOSAA.24.002175>.
- Nowakowski, M., Sheehan, M., Neal, D., & Goncharov, A. (2012). Investigation of the isoplanatic patch and wavefront aberration along the pupillary axis compared to the line of sight in the eye. *Biomedical Optics Express*, 3(2), 240–258, <https://doi.org/10.1364/BOE.3.000240>.
- Ogboso, Y., & Bedell, H. (1987). Magnitude of lateral chromatic aberration across the retina of the human eye. *Journal of the Optical Society of America A*, 4(8), 1666–1672, <https://doi.org/10.1364/JOSAA.4.001666>.
- Ortiz, S., Pérez-Merino, P., Gamba, E., de Castro, A., & Marcos, S. (2012). In vivo human crystalline lens topography. *Biomedical Optics Express*, 3(10), 2471–2488, <https://doi.org/10.1364/BOE.3.002471>.
- Patino, C., McKean-Cowdin, R., Azen, S., Allison, J., Choudhury, F., & Varma, R. (2010). Central and peripheral visual impairment and the risk of falls and falls with injury. *Ophthalmology*, 117(2), 199–206.e1, <https://doi.org/10.1016/j.ophtha.2009.06.063>.

- Polans, J., Jaeken, B., McNabb, R., Artal, P., & Izatt, J. (2015). Wide-field optical model of the human eye with asymmetrically tilted and decentered lens that reproduces measured ocular aberrations. *Optica*, 2(2), 124, <https://doi.org/10.1364/OPTICA.2.000124>.
- Pomerantzef, O., Fish, H., Govignon, J., & Schepens, C. (1971). Wide angle optical model of the human eye. *Annals of Ophthalmology*, 3(8), 815–819.
- Porter, J., Guirao, A., Cox, I., & Williams, D. (2001). Monochromatic aberrations of the human eye in a large population. *Journal of the Optical Society of America A*, 18(8), 1793–1803.
- Pusti, D., Kendrick, C., Wu, Y., Ji, Q., Jung, H., & Yoon, G. (2023). Widefield wavefront sensor for multidirectional peripheral retinal scanning. *Biomedical Optics Express*, 14(8), 4190–4204, <https://doi.org/10.1364/BOE.491412>.
- Roorda, A., Cholewiak, S., Bhargava, S., Ivzan, N., LaRocca, F., Nankivil, D., . . . Banks, M. (2023). The visual benefits of correcting longitudinal and transverse chromatic aberration. *Journal of Vision*, 23(2), 3, <https://doi.org/10.1167/jov.23.2.3>.
- Rosales, P., Dubbelman, M., Marcos, S., & van der Heijde, R. (2006). Crystalline lens radii of curvature from Purkinje and Scheimpflug imaging. *Journal of Vision*, 6(10), 1057–1067, <https://doi.org/10.1167/6.10.5>.
- Rozema, J., Atchison, D., & Tassignon, M. (2011). Statistical eye model for normal eyes. *Investigative Ophthalmology and Visual Science*, 52(7), 4525–4533, <https://doi.org/10.1167/iovs.10-6705>.
- Rozema, J., Rodriguez, P., Navarro, R., & Tassignon, M. (2016). SyntEyes: A higher-order statistical eye model for healthy eyes. *Investigative Ophthalmology and Visual Science*, 57(2), 683–691, <https://doi.org/10.1167/iovs.15-18067>.
- Rucci, M., & Victor, J. (2018). Perspective: Can eye movements contribute to emmetropization? *Journal of Vision*, 18(7), 1–6, <https://doi.org/10.1167/18.7.10>.
- Rynders, M., Lidkea, B., Chisholm, W., & Thibos, L. N. (1995). Statistical distribution of foveal transverse chromatic aberration, pupil centration, and angle psi in a population of young adult eyes. *Journal of the Optical Society of America A*, 12(10), 2348–2357, <https://doi.org/10.1364/josaa.12.002348>.
- Safran, A., Mermillod, B., Mermoud, C., de Weisse, C., & Desangles, D. (1993). Characteristic features of blind spot size and location, when evaluated with automated perimetry: Values obtained in normal subjects. *Neuro-Ophthalmology*, 13(6), 309–315, <https://doi.org/10.3109/01658109309044579>.
- Sankaridurg, P., Donovan, L., Varnas, S., Ho, A., Chen, X., Martinez, A., . . . Holden, B. (2010). Spectacle lenses designed to reduce progression of myopia: 12-month results. *Optometry and Vision Science*, 87(9), 631–641, <https://doi.org/10.1097/OPX.0b013e3181ea19c7>.
- Schwiegerling, J. (2002). Scaling Zernike expansion coefficients to different pupil sizes. *Journal of the Optical Society of America A*, 19(10), 1937–1945.
- Schwiegerling, J. (2004). *Field guide to visual and ophthalmic optics*. SPIE Press.
- Schwiegerling, J. (2018). Optical properties of schematic eye models. *Imaging and Applied Optics 2018 (3D, AO, AIO, COSI, DH, IS, LACSEA, LS&C, MATH, PcaOP)*, paper 3Tu5G.2, <https://opg.optica.org/abstract.cfm?URI=3D-2018-3Tu5G.2>.
- Smith, E., Hung, L., & Huang, J. (2009). Relative peripheral hyperopic defocus alters central refractive development in infant monkeys. *Vision Research*, 49(19), 2386–2392, <https://doi.org/10.1016/j.visres.2009.07.011>.
- Smith, W. (2000). *Modern optical engineering: The design of optical systems* (3rd ed). McGraw-Hill.
- SOMO optical. (2022). *Finished lens catalogue*. Retrieved from: <https://somooptical.com/technical/technical-finished/>.
- Suheimat, M., Zhu, H., Lambert, A., & Atchison, D. (2016). Relationship between retinal distance and object field angles for finite schematic eyes. *Ophthalmic Physiological Optics*, 36(4), 404–410, <https://doi.org/10.1111/opo.12284>.
- Thibos, L., Bradley, A., Liu, T., & López-Gil, N. (2013). Spherical aberration and the sign of defocus. *Optometry and Vision Science*, 90(11), 1284–1291.
- Thibos, L., Bradley, A., Still, D., Zhang, X., & Howarth, P. (1990). Theory and measurement of ocular chromatic aberration. *Vision Research*, 30(1), 33–49, [https://doi.org/10.1016/0042-6989\(90\)90126-6](https://doi.org/10.1016/0042-6989(90)90126-6).
- Thibos, L., Hong, X., Bradley, A., & Applegate, R. (2004). Accuracy and precision of objective refraction from wavefront aberrations. *Journal of Vision*, 4(4), 329–351, <https://doi.org/10.1167/4.4.9>.
- Thibos, L., Ye, M., Zhang, X., & Bradley, A. (1992). The chromatic eye: A new reduced-eye model of ocular chromatic aberration in humans. *Applied Optics*, 31(19), 3594–3600.
- Villegas, E., Marín, J., Ginis, H., Robles, C., Alcón, E., Hervella, L., . . . Artal, P. (2022). Peripheral refraction and contrast detection sensitivity in pseudophakic patients implanted with a new meniscus intraocular lens. *Journal of Refractive Surgery*, 38(4), 229–234, <https://doi.org/10.3928/1081597X-20220113-01>.

- Walline, J., Walker, M., Mutti, D., Jones-Jordan, L., Sinnott, L., & Giannoni, A., for the BLINK Study Group. (2020). Effect of high add power, medium add power, or single-vision contact lenses on myopia progression in children: The BLINK randomized clinical trial. *JAMA*, 324(6), 571, <https://doi.org/10.1001/jama.2020.10834>.
- Wallman, J., & Winawer, J. (2004). Homeostasis of eye growth and the question of myopia. *Neuron*, 43(4), 447–468, <https://doi.org/10.1016/j.neuron.2004.08.008>.
- Watson, A., & Ahumada, A. (2008). Predicting visual acuity from wavefront aberrations. *Journal of Vision*, 8(4), 17, <https://doi.org/10.1167/8.4.17>.
- Wei, X., & Thibos, L. (2010). Modal estimation of wavefront aberrations over elliptical pupils from wavefront gradients. *Optometry and Vision Science*, 87(10), E767–E777.
- Winter, S., Sabesan, R., Tiruveedhula, P., Privitera, C., Unsbo, P., Lundström, L., . . . Roorda, A. (2016). Transverse chromatic aberration across the visual field of the human eye. *Journal of Vision*, 16(14), 9, <https://doi.org/10.1167/16.14.9>.
- Wood, J., & Troutbeck, R. (1992). Effect of restriction of the binocular visual field on driving performance. *Ophthalmic and Physiological Optics*, 12(3), 291–298, <https://doi.org/10.1111/j.1475-1313.1992.tb00400.x>.
- Yang, J., Liu, W., Lv, W., Zhang, D., He, F., Wei, Z., . . . Kang, Y. (2013). Method of achieving a wide field-of-view head-mounted display with small distortion. *Optics Letters*, 38(12), 2035–2037, <https://doi.org/10.1364/OL.38.002035>.
- Ye, M., Bradley, A., Thibos, L., & Zhang, X. (1991). Interocular differences in transverse chromatic aberration determine chromostereopsis for small pupils. *Vision Research*, 31(10), 1787–1796, [https://doi.org/10.1016/0042-6989\(91\)90026-2](https://doi.org/10.1016/0042-6989(91)90026-2).
- Zapata-Díaz, J., Radhakrishnan, H., Charman, W., & López-Gil, N. (2019). Accommodation and age-dependent eye model based on in vivo measurements. *Journal of Optometry*, 12(1), 3–13, <https://doi.org/10.1016/j.optom.2018.01.003>.
- Zemax OpticStudio 20.3 User Manual*. (2020).

## Appendix A: Elaboration of input wavefront error data

This section describes the wavefront error data that were obtained from five previous studies and used to optimize the individual eye models. Details of the instrument system, measurement field locations, and

subject demographics are included. The interested reader is also directed to the original publications for further elaborations of the respective Methods. Each study accounted for the elliptical pupil shape in their off-axis measurements; different methods of this adjustment have been shown to not differ substantially (Lundström, Gustafsson, & Unsbo, 2009; Wei & Thibos, 2010). The visual field sign conventions used in each of the contributing studies have been converted to the convention defined in the Methods of this paper for right eyes.

### Lundström et al., Journal of Vision, 2009

Five emmetropic right eyes (age range, 25–36 years) from Lundström et al. (2009) were considered; their myopic eyes were not included because they were measured while wearing spectacle corrections. They defined emmetropia as a “spherical refractive error between  $\pm 0.5$  D and maximum astigmatism of 0.5 D.” Wavefront error data were measured without cycloplegia using a custom 780-nm open-field Shack-Hartmann device (Mira-Agudelo, Lundström, & Artal, 2009). Field positions spanned  $-40^\circ$  to  $+40^\circ$  in the horizontal visual field and  $-20^\circ$  to  $+20^\circ$  in the vertical field in  $10^\circ$  increments. Zernikes were fit “over a circular aperture that encircled the true pupil.”

### Mathur, Charman, & Atchison., Journal of Vision, 2009

Wavefront error data from nine emmetropic right eyes (age range, 21–30 years) were considered from Mathur et al. (2009), which were measured at 38 field locations that covered  $42^\circ$  (horizontal)  $\times$   $32^\circ$  (vertical) of the central visual field. A COAS-HD wavefront sensor (Johnson & Johnson Vision, Santa Ana, CA) was used, which output aberrations at 555 nm. Eccentric measurements through elliptical pupils were adjusted (Atchison, Scott, & Charman, 2007) by expanding the elliptical pupil along its minor axis until it is circular, and then fitting Zernike coefficients over the resultant circular pupil.

### Polans et al., Optica, 2015

Polans et al. (2015) pooled two sets of data measured using a custom Shack-Hartmann device (Jaeken et al., 2011a) that operated at 780 nm. Their first dataset was only measured along the horizontal field meridian; we did not consider those data. Their second dataset included measurements across  $-40^\circ$  to  $+40^\circ$  in the horizontal field and  $-25^\circ$  to  $+25^\circ$  in the vertical field,

in increments of 1° and 5°, respectively. This second dataset consisted of 10 right eyes (the mean ± standard deviation age of both datasets pooled was 27.5 ± 7.2 years. Data from the horizontal field direction were included in 5° increments (rather than the 1° increments in which they were measured). Measurements over elliptical pupils were unwrapped and rescaled to a circular 4-mm diameter (Lundström et al., 2009).

**Liu and Thibos, Journal of Vision, 2016**

Using a custom Shack–Hartmann wavefront sensor (Liu et al., 2016) that operated at 850 nm, Liu and Thibos measured 16 emmetropic and 18 myopic left eyes (age ranges were 19–36 years and 20–32 years, respectively). Wavefront error measurements were recorded without cycloplegia at approximately 37 field locations radially arranged around fixation spanning a circular field of 27°. Zernike polynomials for off-axis measurement were fit over a circular domain circumscribed to the elliptical pupil (Wei & Thibos, 2010).

**Biomedical optics express, Pusti et al., 2023**

A custom wavefront sensor (Jung, Ghosh, & Yoon, 2015; Pusti et al., 2023) operating at 850 nm was used to measure left eyes along 0°, 45°, 90°, and 135° radial orientations including –30° to +30° horizontally, –18° to +18° vertically, and –10° to +10° obliquely. Those wavefront errors were reported at a 5.5-mm pupil diameter.

**Appendix B: Cauchy dispersion coefficients for refractive media of the models**

Atchison and Smith (Atchison & Smith, 2005) report Cauchy’s 1836 equation as

$$n(\lambda) = A + \frac{B}{\lambda^2} + \frac{C}{\lambda^4} + \frac{D}{\lambda^6} + \dots, \quad (A1)$$

	Cornea	Aqueous	Lens surface	Lens center	Vitreous
A	1.362994	1.323031	1.356086	1.40965	1.323757
B	6,009.687	6,070.796	6,428.455	6,521.218	55,60.24
C	–676,076,000	–706,230,500	–602,373,800	611,066,000	–581,739,100
D	5.90845E+13	6.14786E+13	5.82415E+13	5.90819E+13	5.03681E+13

Table A1. Cauchy equation coefficients used in the modeling.

where  $n$  is the effective refractive index as a function of wavelength ( $\lambda$ ) in nanometers, and coefficients  $A$ ,  $B$ ,  $C$ , and  $D$  are given for the various ocular media in their Table 5. The Cauchy equation coefficients used in the present modeling are tabled below (Table A1) and are essentially those from Table 3 of Navarro (2014).

**Appendix C: Conversion of Cauchy dispersion coefficients to Zemax extended formula**

Zemax OpticStudio defines their extended formula as:

$$n^2 = a_0 + a_1\lambda^2 + \frac{a_2}{\lambda^2} + \frac{a_3}{\lambda^4} + \frac{a_4}{\lambda^6} + \frac{a_5}{\lambda^8} + \frac{a_6}{\lambda^{10}} + \frac{a_7}{\lambda^{12}}, \quad (A2)$$

where  $\lambda$  is wavelength in micrometers.

The conversions from Cauchy to Zemax extended formula coefficients are as follows:

$$\begin{aligned} a_0 &= A^2 \\ a_1 &= 0 \\ a_2 &= (2AB)/(1000^2) \\ a_3 &= (B^2 + 2AC)/(1000^4) \\ a_4 &= (2AD + 2BC)/(1000^6) \\ a_5 &= (C^2 + 2BD)/(1000^8) \\ a_6 &= (2CD)/(1000^{10}) \\ a_7 &= (D^2)/(1000^{12}) \end{aligned}$$

The denominators in  $a_2$  through  $a_7$  are necessary because the two equations define wavelength using different units (nanometers versus micrometers).

**Appendix D: Equations for the calculation of dioptric defocus from Zernike aberration coefficients**

Most of the article presents a computation of dioptric defocus that includes primary and secondary

spherical aberrations with second-order defocus (Thibos et al., 2004):

$$M = \frac{-4\sqrt{3}C_4 + 12\sqrt{5}C_{12} - 24\sqrt{7}C_{24}}{r^2}. \quad (\text{A3})$$

Figure 6 includes dioptric defocus computed using second-order defocus alone:

$$M = \frac{-4\sqrt{3}C_4}{r^2}. \quad (\text{A4})$$